Longer-term terrestrial responses in the aftermath of the end-Cretaceous mass extinction

J. Y. Wang[1], X. H. Li[1], Y. X. Li[1], Y. Wang[2], and C. Y. Zheng[1]

[1]State Key Laboratory of Mineral Deposit Research, School of Earth Sciences and Engineering Nanjing University, Nanjing 210023, China

[2]East China Mineral Exploration and Development Bureau of Jiangsu Province, Nanjing 210007, China

Corresponding author: Xianghui Li (seanlee@nju.edu.cn)

Key Points (each 140 characters limit):

- Terrestrial carbon isotope and pCO_2 vibrate by collapse, smooth and rebound in 1.5 million years after Cretaceous/Paleogene boundary
- With similar pattern in surface ocean, vibrations unravel a process of deterioration, stabilization and recovery of global ecosystem
- Terrestrial and surface ocean systems experienced more unstable, difficult and erratic recovery process than in deep ocean system

Abstract

Mass-extinction with instantaneous and short-term effects on extreme climate and deteriorated ocean environment across the Cretaceous/Paleogene boundary (K/PgB) has been verified by an array of geological records, however, a longer-term (~100−1000 Kyr) post-K/PgB variation remains poorly understood, particularly due to the scarcity of terrestrial records. This study presents carbon isotope analysis of pedogenic carbonates in the Nanxiong Basin, South China to reconstruct carbon cycles and atmospheric CO_2 concentrations (pCO_2) spanning 70.0–62.0 Ma. Combined with data from Songliao Basin (China) and Tornillo Basin (USA), $\delta^{13}C$ displays a post-K/PgB (66.0-64.5 Ma) vibration that is correlative to the surface ocean but mirroring to the bottom ocean. The vibration shows a pattern of collapse and smooth towards rebound, constituting a process of ~400 Kyr (millennia) deterioration, ~300 Kyr stabilization and ~800 Kyr recovery for the longer-term ecosystem and environment. A similar pattern is observed for the reconstructed pCO_2, correlating to changes of sea surface temperature (SST) but contrasting bottom water temperature (BWT). With the discrepancy of longer-term proxy variations, it is proposed that ecosystems and environments in terrestrial and surface ocean had experienced a more unstable, difficult and erratic recovery process and were much more sensitive to climatic changes than in deep ocean for ~1.5 million years in the aftermath of the end-Cretaceous mass extinction. In addition, the decoupling of proxy variations from expected effects implies Deccan volcanism and Chicxulub impact may not have played a key role in the longer-term CO_2 perturbation and environmental change following the K/PgB.

Keywords: pedogenic carbonate; carbon cycle; atmospheric CO_2 concentration; ecosystem; climatic perturbation; Cretaceous-Paleogene boundary

Plain Language Summary

The end-Cretaceous mass extinction is well known for the demise of non-avian dinosaurs at ~66 Ma (million years ago). The instantaneous (< ~1.0 Kyr; thousands years) extreme changes of environment and climate with the mass extinction have been attributed to the Chicxulub impact and recently linked to the Indian Deccan volcanism. However, longer-term (>100 Kyr) changes of environmental and climatic conditions across the Cretaceous/Paleogene boundary (K/PgB) remain poorly understood, especially in terrestrial realm. In this paper, a terrestrial record from South China combined with data from Northeast China and America is presented to decipher climate conditions using carbon isotope ($\delta^{13}C$) of pedogenic carbonates and estimated atmospheric CO_2 concentration (pCO_2). Results show that $\delta^{13}C$ and pCO_2 changes are characterized by collapse, smooth and rebound spanning ~1.5 million years after the K/PgB, indicating the deterioration, stabilization and recovery of terrestrial ecosystem. With correlatability in surface sea and mirroring in deep ocean, terrestrial and surface ocean ecosystems probably experienced a more difficult and erratic recovery process than deep water, appearing at odds with the expected effects of geological events, suggesting Chicxulub impact and Deccan volcanism may not have played the key role in longer-term CO_2 perturbation and environmental change.

1. Introduction

As one of the five largest mass extinctions of the Phanerozoic (e.g., Keller, 1988, 2014), the end-Cretaceous mass extinction is best known for the demise of non-avian dinosaurs. The Chicxulub asteroid impact and Deccan volcanism have been speculated as crucial events that drove climate deterioration (e.g., Alvarez, et al., 1980; Hildebrand et al., 1991; Nordt et al., 2002; 2003; Vajda et al., 2003; Keller, 2014; Keller et al., 2012, 2020; Barnet et al., 2018; Zhang et al., 2018; Gilabert et al., 2021b) and the mass extinction (e.g., MacLeod et al., 1998; Schulte et al., 2010; Renne et al., 2015; Hull et al., 2020; and references therein), even though the precise driving mechanism and the role that each event played in the mass extinction are still strongly debated (e.g., Keller et al., 2016; Percival et al., 2018; Sprain et al., 2019; Dzombak et al., 2020; Gilabert et al., 2021a, b).

Consequently, transient (< ~1 Kyr, millennia years) deterioration and recovery of ecosystem, environment and climate immediately following the Cretaceous/Paleogene boundary (K/PgB) have been well illustrated in marine environment anomalies in temperature (e.g., Vellekoop et al., 2016; Woelders et al., 2017; Barnet et al., 2018), bioproductivity (e.g., Donovan et al., 2016; Henehan et al., 2016), surface ocean acidification (D'Hondt et al., 1994; Kring, 2007; Ohno et al., 2014; Tyrrell et al., 2015; Hart et al. , 2019; Henehan et al. 2019), methane emission (Beerling et al 2002), extinction of pelagic calcifiers (e.g., D'Hondt and Keller, 1991; Bown, 2005), food web collapse (Coccioni and Marsili, 2007), carbonate dissolution (Coccioni et al., 2012; Henehan et al., 2016); and also in the terrestrial realm by biota (e.g., Vajda et al., 2001; Wilf et al., 2003; Coccioni and Marsili, 2007), geochemistry (e.g., Sepúlveda e al., 2009; Nordt et al., 2011; Gao et al., 2021), carbon and oxygen isotopes (Nordt et al., 2002, 2003; Gao et al., 2015; Zhang et al., 2018), subaerial temperature (Nordt et al., 2003; Dworkin et al., 2005; Zhang et al., 2018), atmospheric CO_2 concentrations (i.e. the partial pressure, pCO_2; e.g., Arens et al., 2000; Nordt et al., 2002, 2003; Gao et al., 2015), magnetic susceptibility (Ma et al., 2018), total Hg/TOC ratios (e.g., Keller et al., 2020; Zhao, et al., 2021; Gu et al. 2022; Ma et al., 2022), and so on.

On the other hand, a longer-term (~100−1000 Kyr interval) environment and climate change in the aftermath of the end-Cretaceous mass extinction has not been extensively explored due to the lack of suitable materials, leading to a poor understanding of intrinsic linkages in global environment and climate changes to causal mechanism. To date, there are few examples of climatic proxy analysis from higher-resolution terrestrial records at a longer-term timescale, albeit high-resolution stable isotope analyses of foraminifera-dominated tests were recently made across the K/PgB through the main Paleocene (-Eocene) and the orbitally forcing of marine carbon cycles was proposed to interpret the oceanic and climatic conditions and origins (e.g., Coccioni et al., 2012; Hollis et al., 2012; Littler et al., 2014; Zeebe et al., 2017; Barnet et al., 2018, 2019; Gilabert et al., 2021b) and relatively less research of surface ocean with relevant proxies can be also found using planktonic foraminifera (Keller and Lindinger, 1989), nannoplankton (Eldrett et al., 2021), and bulk carbonate (Coccioni et al. 2012; Hull et al., 2020).

Stable isotope analysis and estimation of pCO_2 are useful for understanding the driving mechanisms behind changes in paleoclimates and paleoenvironments. These techniques have

been widely applied in deep time paleoclimate reconstructions, particularly for greenhouse climates of the Cretaceous–Paleogene. The carbon isotopic composition ($\delta^{13}C$) of pedogenic carbonate is an important climate proxy for the terrestrial ecosystem and has been adopted to reconstruct pCO_2 (e.g., Cerling, 1991, 1999; Breecker & Sharp, 2008; Breecker et al., 2009). This proxy has been utilized extensively to calculate pCO_2 during the Cretaceous (e.g., Lee et al., 1999; Robinson et al., 2002; Sandler, 2006; Huang et al., 2012; Li, X.H. et al., 2014; Li, J. et al., 2016; Harper et al., 2021) and in a short time interval after the K/PgB (e.g., Nordt et al., 2002, 2003; Huang et al., 2013; Gao et al., 2015, 2021; Zhang et al., 2018). The latter provide some important insights into the driving mechanisms and short-term (<~500 Kyr) climate change around the K/PgB. However, few proxies extending to 3-5 Myr interval were reported and applied to analyze terrestrial environment and climate after the K/PgB event.

Calcic paleosols are commonly preserved in terrestrial basins, arid zone on the earth (Fig. 1). Calcisols are widespread in the Cretaceous basins of South China (Li et al., 2009) and especially abundant in the Upper Cretaceous sediments of the Nanxiong Basin, where continuous K/PgB successions are exposed (Fig. 2), with good age constraints of biostratigraphy and magnetostratigraphy. Here we use pedogenic carbonate $\delta^{13}C$ records from the Nanxiong Basin to explore longer-term carbon isotopes and estimate pCO_2 concentration at a higher resolution. We further combine our new results with published data from the Songliao Basin in northeast China and Tornillo Basin (Big Bend National Park), Texas, USA (Fig. 1) to decipher terrestrial responses to the global carbon cycle perturbation in the aftermath of the end-Cretaceous mass extinction.

2. Stratigraphy and age constraints

The chronostratigraphy of the uppermost Cretaceous–lowermost Paleocene in the Nanxiong Basin, Guangdong province, South China, has been constructed in a number of biostratigraphy, lithostratigraphy, magnetostratigraphy and stable isotope studies (e.g., Zhao et al., 1991; Erben et al., 1995; Zhang et al., 2006; Clyde et al., 2010; Li et al., 2010; Tong et al., 2013; Zhang and Li, 2010). In particular, the evolution of mammals and reptiles such as non-avian dinosaurs (e.g., Zhao et al., 1991, 2009; Clyde et al., 2010), along with the magnetostratigraphy (e.g., Erben et al., 1995; Clyde et al., 2010), have been primarily used to date the strata. The uppermost Zhutian and Zhenshui formations have been dated as the late Campanian–Maastrichtian, comprising polarity chrons 31R to 29R. The overlying Shanghu Formation (Pingling Member + Xiahui Member) has been dated as the Danian (early Paleocene) in age, comprising polarity chrons from upper 29R to 27R (Fig. 3). The sedimentary sequence of the Datang section has an absolute age range of ~9.2 million years, spanning ~71.4–62.2 Ma based on the International Chronostratigraphic Chart (Cohen et al., 2013, 2022) and by correlating polarity chrons to absolute age (Ogg et al., 2012; Vandenberghe et al., 2012). All the beds and thicknesses of the section are adopted from Zhang et al. (2006) in this paper, and those with paleosol horizons span ~8.0 (70.0−62.0 Ma) Myr.

Well constrained by magnetostratigraphy (Clyde et al., 2010), the bottom ages of magneto-chrons 31N, 30R, 30N, 29R, 29N, 28R, 28N and 27R are assigned 69.4 Ma, 67.6 Ma,

67.4 Ma, 66.6 Ma, 65.7 Ma, 64.9 Ma, 64.6 Ma and 63.5 Ma following the chronostratigraphic chart (Ogg et al., 2012; Vandenberghe et al., 2012), corresponding to the depth of 74.1 m, 142.5 m, 234.7 m, 271.3 m, 459.5 m, 492.2 m, 618.0 m and 641.9 m in the Datang section (Zhang et al., 2006), respectively (Fig. 3). These well-dated depths are key for the age determination of calcrete samples, for which interpolation criterion between two neighboring boundary ages was used to constrain the age of individual sample.

Nevertheless, a problem involves the placement of the K/PgB within the sedimentary section. As summarized by Zhang et al. (2006), there are about four potential candidates for the placement of the K/PgB. The most popular potential candidates include between Bed 41 and 42 or between Bed 42 and 43, based on the disappearance of dinosaur fossils and magnetostratigraphy. Alternatively, the K/PgB could be placed between Bed 48 and 49 based on the first appearance of the mammal genus *Bemalambda*. Zhang and Li (2015) suggest that the entire Pingling Member is of the latest Cretaceous age based on biostratigraphy, although the disappearance of dinosaur fossils occurs in the lowest horizons of this member in their studied sections. By integrating the magnetostratigraphy, disappearance of dinosaur fossils (e.g., Zhang et al., 2006; Clyde et al., 2010) and fluctuations in the Hg/TOC ratio (Zhao et al., 2021), we adopt the K/PgB at the boundary between Bed 42 and Bed 43 in this study. The K/PgB position basically represents the end-Cretaceous mass-extinction even if it is possible that this position could not be precisely followed the original definition K/PgB with the Chicxulub impact time. It is noted that Bed 42 is only 1.7 m thick, whatever the K/PgB is placed between Bed 42 and 43 or Bed 41 and 42 insignificantly influences the deciphering of carbon isotope and pCO_2 trends.

In addition, the major part of Bed 21 in the Lower Member of the Zhenshui Formation is covered by farmland. Ma et al. (2018) considered this unexposed section encompassed two polarity chrons (30R and 31N), proposing an alternative of 31R, 32N.1n, and 32N.1r for the underlying Zhutian Formation and an age of 71.5 Ma for the boundary between the Zhenshui and Zhutian formations. As it is not confirmed yet, in this manuscript, we still use the former age classification by Zhang et al. (2006) and Clyde et al. (2010), i.e., Bed 21 encompasses the upper chron 30R.

With an uncertainty of ~0.1–0.05 Myr, the age model matches the well-constrained interval within the Songke #1 well in Songliao Basin, northeast China (Gao et al., 2015; Zhang et al., 2018; and references therein) and the Tornillo Basin, USA (e.g., Nordt et al., 2003).

3. Materials and methods

3.1. Determination of paleosols

There are multiple classifications of paleosols (e.g., Wright, 1992; Mack et al., 1993; Retallack, 2001; Imbellone, 2011), which are mostly based on the US Soil Taxonomy (Soil Survey Staff, 1998). In our study, we use the paleosol classification of Mack et al. (1993) and Retallack (2001).

For paleosol determination, detailed field observations were made. We recognized paleosols based on multiple properties and features including 1) color, 2) lithological (fine) texture; 3) soil structure, 4) destratification and horizonation, 5) root traces, 6) particularities of mottles, slickensides, and leaching, 7) composition of B horizon, 8) pedogenic nodules, and 9) exposure markers, among other factors.

3.2. Diagenetic diagnosis of calcrete samples

We used several methods to examine the amount of diagenetic alteration of pedogenic carbonate (calcrete) samples before powder drilling.

The field occurrence of calcretes is a relatively direct diagnosis of diagenesis. Petrographic observations of thin-sections under the optical microscope also greatly help to interpret diagenesis. We made thin-sections for most of the samples.

Cathodoluminescence (CL) imaging is a common technique for assessing the degree of diagenetic alteration of a carbonate sample. CL imaging is also a common and valid method for examining potential diagenetic modification of pedogenic calcretes. Representative calcrete samples were scanned by a CL electron microscope and imaged. The covariance of carbon and oxygen isotope values can also be used to characterize the extent of diagenetic alteration, in which a high R^2 or R value could indicate significant diagenesis.

3.3. Powdering of samples and measurement of carbon-oxygen isotopes

Powdered samples of micritic calcites were acquired using a dental drill (aiguille diameter ø1–2 mm). Drilling was focused on a small point comprising a hard and even calcified area, avoiding any sparry calcite filling cracks, veins, and vugs. 0.2–0.4 mg of powdered sample was prepared for carbon and oxygen isotope analysis. Samples with A and B letters at the end of the numbers represent duplicate samples from the same calcrete to test reproducibility (Table S1). 159 analyses from 96 pedogenic carbonate samples (representing 96 corresponding calcisols) were performed, including duplicate analyses for some samples (Table S1 and Fig. 3).

The powder was then placed in an oven for drying at 60℃ for 10 hours before being moved to the sample vials. Carbon dioxide gas was produced from the sample by adding orthophosphoric acid at 70℃, while isotopic analysis was performed using a DELTA-Plus XP (CFIRMS) mass spectrometer. Analyses were carried out at the State Key Laboratory for Mineral Deposits Research, Nanjing University. Instrument precision was regularly checked using the Chinese national carbonate standard GBW04405 and the international standard NBS19, equating to $<\pm 0.1‰$ for $\delta^{13}C$ and $\delta^{18}O$ (1σ). Data were calibrated to the international Vienna Pee Dee Belemnite (VPDB) scale using the NBS19 and NBS18 standards.

3.4. Calculation of pCO_2

Reconstructions of pCO_2 from pedogenic carbonate carbon isotope data in deep time (pre-Quaternary) are based on two principal assumptions: 1) soil-respired CO_2 was not

produced by C4-plants, and 2) soil CO_2 has a constant carbon isotope composition. The validity of these two assumptions for paleosol records from the pre-Quaternary has been verified (e.g., Cerling, 1991, 1999; Ekart et al., 1999; Retallack 2001, 2005).

An empirical equation for pCO_2 concentration has been developed by Cerling (1999) and improved by Ekart et al. (1999):

$$C_a = S_{(z)} (\delta^{13}C_s - 1.0044\ \delta^{13}C_r - 4.4) / (\delta^{13}C_a - \delta^{13}C_s) \quad [1]$$

where C_a is the atmospheric pCO_2 (ppmV) concentration we are calculating, $S_{(z)}$ is the soil pCO_2 concentration (ppmV), and $\delta^{13}C_s$, $\delta^{13}C_r$, and $\delta^{13}C_a$ represent the stable carbon isotope compositions of soil pCO_2, soil-respired pCO_2, and atmospheric pCO_2, respectively.

In more detail, there are two ways to calculate C_a. One way assumes that $S_{(z)}$ is a constant value, while the other assumes that $S_{(z)}$ changes with soil depth. In the second method, $S_{(z)}$ is a function of the thickness of the overburden strata (soil burial depth) to the Bk horizon. This method has been applied to the Quaternary soils (e.g., Retallack, 2009; Breecker and Retallack, 2014) and partly to the Cretaceous soils (e.g., Huang et al., 2013; Gao et al., 2015; Li et al., 2016; Zhang et al., 2018). However, since it is quite difficult to apply a soil burial depth factor for pre-Cenozoic soils, we used the first method to estimate C_a using a constant value for $S_{(z)}$ in this study.

Around ten years ago, values of 4000−5000 ppmV were commonly selected for $S_{(z)}$. However, more and more evidence indicates that $S_{(z)}$ changes with the degree of aridity or humidity, with 1000−1500 ppmV and 2000−2500 ppmV considered to be reasonable values for $S_{(z)}$ in arid to semi-arid soils and semi-arid to semi-humid soils, respectively (e.g., Brook et al., 1983; Khadkikar et al., 2000; Breecker et al., 2009, 2010). Therefore, we used a value of $S_{(z)}$ = 2000 ppmV to estimate pCO_2 concentrations from pedogenic carbonate in this study, since the Nanxiong, Songliao and Tornillo basins were all located in the northern Hemisphere (semi-) arid zone during the Late Cretaceous and early Paleogene (Fig. 1).

$\delta^{13}C_s$ can be calibrated either with the formula $\delta^{13}C_s = -8.98 + \delta^{13}C_c$ (Ekart et al., 1999), or with $\delta^{13}C_{sc} = (\delta^{13}C_c + 1000) / ((11.98 - 0.12 * T) / 1000 + 1) - 1000$ at 25°C (Romanek et al., 1992), where $\delta^{13}C_c$ is the carbon isotope value of pedogenic carbonate measured in lab. We used the two formula to calibrate the $\delta^{13}C_s$ in this work, and the results show no distinct differences in the resulting calculated pCO_2 concentrations (<10% in error, mostly 3−5%. See Table S1 and S2).

$\delta^{13}C_r$ can often adopt the coeval organic carbon isotope composition ($\delta^{13}C_{om}$) of marine and terrestrial sediments. Unfortunately, no high-resolution and high-precision $\delta^{13}C_{om}$ values are currently available for the late Maastrichtian−early Paleocene. We therefore need to use an alternative approach to calculate $\delta^{13}C_r$. Firstly, we can use the transfer function of nannoplankton $\delta^{13}C_m$ to obtain $\delta^{13}C_a$ through the equation $\delta^{13}C_a = \delta^{13}C_m - 7.9$ (Thibault et al., 2012), in which the isotopic equilibrium fractionation value between ocean and pCO_2 was assumed (Passey and Cerling, 2002). Secondly, the $\delta^{13}C_{om}$ can be calculated from the equation $\delta^{13}C_a = (\delta^{13}C_{om} + 18.67) / 1.1$ (Arens et al., 2000). Thirdly, the $\delta^{13}C_r$ is calculated by subtracting 1‰ from the calculated value of $\delta^{13}C_{om}$ (Breecker and Retallack, 2014). We obtained values of three parameters from this process: $\delta^{13}C_{om}$, $\delta^{13}C_a$, and $\delta^{13}C_r$. To calculate

these parameters in this study, we chose the nannoplankton $\delta^{13}C_m$ from the Shearwater SW A9 well, central North Sea (Eldrett et al., 2021), which has a relatively complete sequence and high-resolution sampling.

All pCO_2 concentration estimates can be found in supplementary Tables S1 and S2 and Fig. 3. It should be noted that we not only calculated new pCO_2 estimates for the latest Cretaceous–early Paleocene pedogenic carbonates from Nanxiong basins, but also recalculated pre-existing estimates from the Songliao Basin, NE China (Gao et al., 2015; Zhang et al., 2018) and Tornillo Basin, USA (Nordt et al., 2003), uniformly using the same process described above.

Furthermore, carbon and oxygen isotope data from marine sediments were compiled, and temperatures estimated from oxygen isotope of foraminifera and nannoplankton were recalibrated with refined ages (details see supplementary Text S1 and Table S3).

4. Results

4.1 characteristics of paleosols

Field observations show that paleosols are mainly reddish brown, although a few are brownish red and violet red in color, and they were developed in silty/calcareous (occasional gravelly) mudrocks. Calcretes, destratification and slickensides are common in the paleosols, while root traces, mottles and leaching are sometimes associated with mudcracks. Our calcrete samples consisted of hard calcified nodules comprising argillaceous micritic calcite, with a ginger-like, globular, irregular shape and sporadically dispersed occurrence, indicating minimal diagenesis (Fig. 4A and 4B). The observed paleosols are calcisols within the Bk horizon of aridisol and are matured in the IV–VI stage (Machette, 1985).

We observed that the calcrete samples comprise argillaceous micritic calcite with a homogeneous texture and composition, lacking any visible carbonate grains or evidence for carbonate replacement and recrystallization. CL images reveal that most of the samples are dull-luminescent and a few are a homogeneous weak orange, verifying a primary origin (Fig. 4C and 4D).

4.2 Carbon and oxygen isotopes of paleosols

Our $\delta^{13}C$ and $\delta^{18}O$ values display a very low linear covariance $R^2 = 0.0145$ and a binomial quadratic covariance of $R^2 = 0.0527$ (Fig. 5). The low covariance indicates that $\delta^{13}C$ and $\delta^{18}O$ values are independent of each other and demonstrates that our calcrete (powder) samples comprise primary carbonate without any significant diagenetic overprint.

$\delta^{13}C$ values range from −12.41‰ to −4.98‰ (mean −8.95‰, gap $\Delta\approx6.5$‰) (Fig. 3 and Table S1), falling the carbon isotope scope of calcisol calcretes. When combined with data from the GCD section, Nanxiong Basin (Clyde et al., 2010), the Songliao Basin (Gao et al., 2015; Zhang et al., 2018) and the Tornillo Basin (Nordt et al., 2003), $\delta^{13}C$ values encompass a similar range with high-frequency fluctuation (Fig. 6B). Meanwhile, further Kernel smoothing of the composite $\delta^{13}C$ data exhibits a different scenario with three phases (Fig. 6B):

I, decrease with slight decrease spanning 70−66 Ma; II, vibration with great fall and rise spanning 66−63.5 Ma; and III, slight increase spanning 63.5−62.2 Ma.

4.3 pCO_2 estimates

pCO_2 varies from ~250 ppmV to ~2500 ppmV (mean 960 ppmV, gap Δ≈ 2000 ppmV) in the Nanxiong Basin (Fig. 3 and Table S1). Combined with pCO_2 estimates from the Nanxiong, Songliao and Tornillo basins, recalculated following the methodology employed in this study, pCO_2 ranges between 251 ppmV and 2555 ppmV (mean 1022 ppmV). Within these data, 91.1% (359 of 394 analyses) fall within the 275−1650 ppmV range, 1−6 times the preindustrial level (275 ppmV). As in the $\delta^{13}C$ record, three corresponding phases of pCO_2 can be differentiated with a minor discrepancy, with slightly rising pCO_2 during phases I and III (Fig. 6C).

Using relevant parameters and the formula developed by Breecker and Retallack (2014), uncertainties and Gaussian error (mean, 1σ) are available (Tables S1 and S2 and Fig. 3). Errors (1σ) of pCO_2 range from 85 ppmV to 845 ppmV with a mean 306 ppmV for this work and 332 ppmV for the combined data. Although average uncertainties are a little bit large, ~30−32% for this work and the combined, respectively, within the uncertainty, it is acceptable for trend analysis of pCO_2. The largest source of the uncertainty is caused by the standard error (766 ppmV) of modern soil carbonate (Breecker and Retallack, 2014). pCO_2 uncertainty will decrease by ~ 20% if half (383 ppmV) of the standard error is selected, and decrease to ~12% when 1/4 (~191 ppmV) standard error is chosen. Another largest source of error is the $S_{(z)}$ value. pCO_2 will fall from ~31% to ~20% in error if $S_{(z)}$=2500 ppmV is selected instead of 2000 ppmV. In addition, the average values of pCO_2 are 719 ppmV, 959 ppmV, and 1199 ppmV for the section when $S_{(z)}$=1500 ppmV, 2000 ppmV, 2500 ppmV, respectively, and it will get uncertainties 25% and 17%. More importantly, parameters of temperature, $\delta^{13}C_r$, $\delta^{13}C_a$, $\delta^{13}C_s$, contribute little to the pCO_2 uncertainty, and the tendency of pCO_2 variations is almost same whatever S(z) selection (Fig. 3).

Occurrences, compositions, CL images and $\delta^{13}C$ and $\delta^{18}O$ value covariances illustrate that calcrete samples have not been significantly altered by diagenesis, and the pedogenic carbonate $\delta^{13}C$ values are suitable for analyses of carbon cycle and estimated pCO_2.

5. Discussion

5.1. Heavy carbon collapse and recovery linking ecosystem variations

Smoothed terrestrial pedogenic $\delta^{13}C$ records from the combination of Nanxiong Basin and other places display three longer-term phases I, II and III (Fig. 6B) and exhibit a significant longer-term vibration of the main Phase II (66.0−64.5 Ma) with three evolutionary stages (II_a, II_b, and II_c) (Figs. 6 and 7), representing the quick shifts in carbon cycle in the aftermath of the end-Cretaceous extinction.

After a moderate increase before the K/PgB, pedogenic carbonate $\delta^{13}C$ decreases immediately by ~6‰ (from −6.2‰ to −12.2‰) during Stage II_a (~66.0−65.6 Ma), indicating a heavy carbon (^{13}C) collapse (HCC) phase. The coeval HCC is also clear in the marine fine

fraction (Keller and Lindinger, 1989), nannoplankton carbonate (Eldrett et al., 2021), benthic foraminifera carbonate (e.g., Hollis et al., 2012; Barnet et al., 2018, 2019) and marine bulk carbonate (Coccioni et al. 2012; Hull et al., 2020), although there could be a little bit age uncertainty (~50 Kyr) for the onset and termination of the HCC phase. It is also distinct that the terrestrial HCC is much larger (~2-3 times) in magnitude than those in marine inorganic and organic $\delta^{13}C$ (Fig. 7). In addition, a negative excursion of $\delta^{13}C$ −1.5‰ to −2.8‰is recorded in the C3 land plants from Western Interior Seaway of North America within ~160 Kyr interval after the K/PgB (Arens and Jahren, 2000) .

The HCC within ~400 Kyr interval in the early aftermath of the end-Cretaceous extinction is evident from both the marine and terrestrial realms, linking carbon cycle in the surface system reservoir with global ecosystem deterioration. The pertinence of HCC in the two realms is firstly originated from large increase in light carbon preserved in marine sediments and paleosols.

In the terrestrial ecosystem, transient carbon and vegetation biomass collapses and recoveries in the order of tens to thousands of years are interpreted as the results of devegeation/deforestation (e.g., Vajda et al., 2001, 2003) or very low primary productivity (Lomax et al., 2004). We herein propose that the devegetation is also responsible for the HCC in a longer-term scale, that is, the devegetation (/deforestation) could have sustained for an interval of ~400 Kyr (the orbital forcing long eccentricity?) lag in the aftermath of the end-Cretaceous extinction, indicating terrestrial ecosystem deterioration while continental weathering had been enhanced (Opdyke and Wilkinson, 1988; Li and Elderfield, 2013).

$\delta^{13}C_s$, the carbon isotope composition of soil pCO_2, determines the pCO_2 estimate while $S_{(z)}$, $\delta^{13}C_a$ and $\delta^{13}C_r$ are relatively constant. And $\delta^{13}C_s$ is further acquired from $\delta^{13}C_c$, which is derived from carbon isotope compositions of rainfall, soil and pore water, an integrating ecological response to vegetation. When devegetation (/deforestation) takes place, light carbon (^{12}C) from rainfall and atmosphere, has to settle in soil and pore water and record in pedogenic carbonate (calcrete), directly leading to negative $\delta^{13}C$ excursion.

Contemporaneously, the HCC occurs in the marine realm, including those of plankton, benthos and carbonate sediments. This could result from the mass extinction of surface-dwelling plankton and partial collapse of the biological pump or massive export reduction of organic (isotopically light) carbon from the surface to deep ocean, leading to the reduction of the surface-to-deep carbon isotope gradient in the oceans while concentration of light carbon in sea-water and negative $\delta^{13}C$ (Figs. 6A and 7A). The process could work in same pose with the negative $\delta^{13}C$ excursion observed in the terrestrial critical zone, while potentially magnifying it within the surface ocean carbon reservoir. Therefore, the ocean carbon cycle appears to couple from atmosphere during the ~400 Kyr interval spanning 66.0−65.6 Ma after the K/PgB, despite the different gradients and extents of $\delta^{13}C$.

In early works (1980s-1990s), the carbon cycle marked a decoupling of surface and deep water records, annihilating and sometimes reversing the vertical gradient, i.e. $\delta^{13}C$ of deep-water benthic foraminifera shows an increase across the K/PgB, while that of planktic foraminifera test and nannofossil record a strong decline, which were accomplished within a transient/moment time interval (< ~100 Kyr) in geological scale. This paradox was firstly

interpreted as the results of a collapse of primary productivity in a lifeless Strangelove Ocean (Alvarez et al., 1980; Hsü and Mackenzie, 1985), and was later modified to represent an incomplete loss of productivity and a strong decline in the biological pump (Living Ocean Model; d'Hondt et al., 1998; Hull and Norris, 2011). Also, other hypotheses were proposed to argue for the contrast carbon cycle and bioevents in marine system, such as Heterogeneous Ocean" (e.g., Hull and Norris, 2011; Alegret et al., 2012; Alegret and Thomas 2013) or geographic heterogeneity (Whittle et al., 2019), methane emission from oceanic slumps (Beerling et al 2002), the effect of extinction of pelagic calcifiers (e.g., D'Hondt and Keller, 1991; Bown, 2005), food web collapse (Coccioni and Marsili, 2007), carbonate dissolution (Coccioni et al., 2012; Henehan et al., 2016).

The hypothesis of surface water acidification with pH decrease or sulphate-rich vapour has been popularly suggested to be a response to the Chicxulub impact and/or Deccan Trap eruption in moment time (e.g., D'Hondt et al., 1994; Ohno et al., 2014; Tyrrell et al., 2015; Hart et al. , 2019; Henehan et al. 2019) and further modeled and verified (e.g., Henehan et al. 2019), consequently leading to the mass extinction across the K/PgB. In deep sea, an enhanced carbonate preservation was observed and attributed to the extinction of pelagic calcifiers that caused carbonate oversaturation of the oceans (see e.g. Alegret & Thomas 2013; Henehan et al., 2019). Similarly, the release of methane hydrates (Beerling et al 2002) is not supported by the lack of a significant negative carbon isotope excursion within deep sea carbonates of this time and the quick methane oxidization would have resulted in expected pCO_2 increase that was not observed in the reconstruction data.

Above hypotheses indicate an instability of marine environment (e.g., Coccioni and Marsili, 2007; Sinnesael et al., 2016; Gilabert et al., 2021) and terrestrial system (e.g., Vajda et al., 2001, 2003; Vajda and McLoughlin, 2007; Gertsch, et al., 2011; Spicer and Collinson, 2014; Donovan et al., 2020), and have been linked to the Chicxulub impact and / or Deccan Trap eruption (e.g., Gertsch, et al., 2011; Keller, 2014; Barnet, et al., 2018; Zhang et al., 2018; Henehan et al., 2019) although there are some oppositional evidence (e.g., Dzombak et al., 2020; Percival et al., 2018; Milligan et al., 2019). However, the instability (collapse) and rapid recovery of ecology and environment took place instantaneously soon after the eruption and impact events, and finished in a geological ultra short-term (< ~1.0 Kyr) interval (e.g., Coccioni and Marsili, 2007; Gertsch et al., 2011; Woelders et al., 2017; Gilabert et al., 2021). These hypotheses may not be eligible for the HCC in a longer term (> ~100 Kyr) duration. Namely, the role of the Chicxulub impact and / or Deccan Trap eruption to the HCCs with ~400 Kyr duration of both global marine and terrestrial systems remains suspected. At least the consecutive great decrease in marine and terrestrial $\delta^{13}C$ is not compatible with the fading pulse eruption (vacancy between 65.85−65.65 Ma) of the Deccan Traps (Fig. 7E. Schoene et al., 2019, 2021).

In Stage II_b, the $\delta^{13}C$ values show a smoothing variation at a lowest level of (surface sea) marine fine fraction ca. −1.5‰ (Keller and Lindinger, 1989), marine bulk carbonate ~1.5‰ (Coccioni et al., 2012) and terrestrial pedogenic carbonate ca. −12‰, spanning ~300 Kyr (~65.6−65.3 Ma). The onset of Stage II_b, also the final of Stage II_a, seems coincident with the cessation of Deccan Traps volcanism, implying the termination of eruptional gas contribution. Thus, a significant positive excursion of carbon isotope would be expected. Nevertheless, we

do not see such a distinct shift in our terrestrial $\delta^{13}C$ record, and so not in the marine counterpart (Fig. 7A and 7B). The regime of (~300 Kyr duration) sustaining lowest $\delta^{13}C$ could be the feedback to the termination of the previous (66.0−65.6 Ma) severe environmental perturbations for a requirement of global stabilization system, before the rapid recovery in the coming stage (II_c), likely corresponding to the DAN-C2 event of carbon redistribution (Quillévéré et al., 2008). The exception of distinct positive shift at ~65.5 Ma, correlatable between marine and terrestrial system (Fig. 7) is suggested an adjustment for the ecosystem stabilization, or an response to a geologic event at the sharp time, perhaps the ALE volcanic ash (Odin et al., 1992).

With the termination of HCC (Fig. 7), $\delta^{13}C$ value quickly increases in a ~800 Kyr span (Fig. 7A and 7B): pedogenic carbonate from ca. −12.0‰ to ca. −6.5‰, marine fine fraction from ca. −1.5‰ to 1.0‰ (Keller and Lindinger, 1989), marine bulk carbonate from ~1.0‰ to 2.5‰ (Coccioni et al., 2012) although there is a little bit uncertainty when $\delta^{13}C$ reaches the pre-K/PgB level. The rapid rebound of carbon isotope indicates the recovery process is closely coherent in both surface marine and terrestrial realms during the interval of ~65.3−64.5 Ma (Phase II_c).

Overall, the pattern of collapse, smooth and rebound process of $\delta^{13}C$ values is quite similar in both surface sea and terrestrial system, suggesting global changes of marine and terrestrial ecosystem and environment. This process is approximately close to those of initial marine biotic shift in abundance and taxonomic richness of benthic molluscan faunas in Antarctica with ~0.32 Myr and ~1.00 Myr period after the K/PgB (Whittle, 2019), respectively.

Surprisingly, $\delta^{13}C$ of benthic foraminifera continuously decreases with a higher extent till 65.2 Ma (Barnet et al., 2018; Norouzi et al., 2021), similar to the framework of the Kernel smoothed curve of the pedogenic carbonate $\delta^{13}C$ (comp. Fig. 6A and 6B), whereas quite different from the pedogenic $\delta^{13}C$ pattern in Stage II_b and II_c (comp. Figs. 7 and 6). And the trend of terrestrial $\delta^{13}C$ also contrast strongly with the slight decrease in deep sea benthic $\delta^{13}C$ after ~65.2 Ma (Barnet et al., 2018). As a whole, $\delta^{13}C$ exhibits variation within the terrestrial realm and surface ocean during the early Paleocene, but display slight change within the deep South Atlantic Ocean (Barnet et al., 2018, 2019).

These discrepancies could result from different ecosystem conditions in water temperature, productivity, nutrition, photosynthesis, etc., where devegetation caused productivity decrease and heavy carbon loss in critical zone and biological pump fading or fail of led to massive export reduction of organic light carbon from surface sea to deep ocean. Therefore, the deep ocean carbon cycle appears to have become decoupled from the surface ocean and atmosphere during the 3 Myr interval spanning 65.3−62.3 Ma in the aftermath of the end-Cretaceous extinction.

5.2. Variations of pCO_2 concentration documenting vibrant climate change

Within the age uncertainties, the estimated pCO_2 shows a quite similar style with the pedogenic carbonate $\delta^{13}C$ (Figs 6 and 7). Three phases can be also recognized, in which four stages are further subdivided for Phase II, with a high degree of variations.

During Stage II_a, pCO_2 steeply declines by ~2000 ppmV (~2500−250 ppmV) spanning ~400 Kyr after a high increase (~800 ppmV) of the pre-K/PgB. This rapid pCO_2 fall was not observed in the Tornillo Basin in North America (Nordt et al., 2003), when the data are calibrated to our age model (Table S2), where biochemical behaviors do not reveal demonstrable changes in soil characteristics (Nordt et al., 2011).

The significant decrease in pCO_2 with albeit six to seven times that of pre-industrial values would expect to have resulted in the coeval global cooling. The mean annual temperature fall ~4°C (Dworkin et al., 2005) supports this cooling tendency on land. Despite this apparent marked decrease in pCO_2, coeval SST (surface sea temperature) fluctuates significantly (Keller and Lindinger, 1989) and exhibit a distinct decrease by ~8°C (32°C to 26°C; Fig. 7D) when use the Kernel smoothed data with the calibrations of age and parameters (Supplementary Text S1 and Table S3). The trend similarity between pCO_2 and SST indicate a rapid climate deterioration commenced shortly after the K/PgB in both the terrestrial realm and surface ocean.

Regardless of the precise age correlation, great falls of pCO_2 and coeval SST would be responses to the cooling, which highly resulted in productivity reduction and devegetation as well as $\delta^{13}C$ negative shift in surface ocean and subaerial systems. During Stage II_a, the Deccan volcanic eruption would instigate an increase in pCO_2 and climatic warming even though only 25% of the Deccan Traps volume in the period (Sprain et al., 2019, 2021), that means pCO_2 and coeval SST would have had a great rise with permanent $\delta^{13}C$ positive shift. The decoupling of climatic proxies from expected effects by volcanic eruption suggests the Deccan Trap volcanism may have not contributed much to the climate change after the Chicxulub impact in a longer-term interval (~400 Kyr soon after the K/PgB). Then, would the bolide impact be responsible for the secular fall of pCO_2 and coeval SST? Our answer is negative.

Following the Chicxulub impact, the absolute abundance of benthic foraminifera increased (Arreguín-Rodríguez et al., 2021) and bottom water temperature (BWT) rose by ~3°C in the tropical Pacific and by 1.5−2°C in the South Atlantic (Jung et al., 2013; Barnet et al., 2018), while SST oscillated between 23−34°C in the south-western Tethys (Keller and Lindinger, 1989). More importantly, dust clouds and possible sulfate aerosols resulting in the impact winter would only circulate within the atmosphere for an extremely short duration, with estimates ranging from less than ten years (Kring, 2003) to millennia at most (Galeotti et al., 2004). These findings suggest that bolide impact exerted a heterogeneous impact on global climate change in an instantaneous time gap, therefore could not have played a causal role in a longer-term (> ~100 Kyr) duration climate change after the K/PgB (Keller et al., 2016). However, it is likely to have played a vital role in destroying the habitats of organisms and perturbing the very short-term carbon cycle in the immediate aftermath of the K/PgB.

In the span of ~65.6−65.3 Ma (Stage II_b), pCO_2 remains at relatively low values of ~250−500 ppmV (Fig. 7B), comparable to those of today, indicating a persistently cool (or even cold) climatic regime. In the deep sea, benthic foraminifera test $\delta^{13}C$ and BWT remain fairly stable without significant change (Fig. 6A and 6D). This roughly happens to the SST in the southern West Tethys (Keller et al., 2016), where SST mainly is stable at 24−26°C with an

514 exception of abrupt rising to ~34°C at ~65.5 Ma (Fig. 7D). The exceptional high SST value is
515 similar with the $\delta^{13}C$ in marine and terrestrial realms, which might be originated by geological
516 event, perhaps the ALE volcanic event (Odin et al., 1992). It is noted that the lowest pCO_2 is
517 often higher than the preindustrial 275 ppmV. Even though 250−275 ppmV can be seen at
518 several intermittences (Fig. 7C), each does not persist for ~100 Kyr, which could not have
519 driven ice cap formation in polar regions.

520 pCO_2 concentration quickly rose by 1400 ppmV (from ~250 ppmV to 1650 ppmV) in
521 ~800 Kyr interval (Fig. 7C), likely indicating rapid warming during the interval of ~65.3-64.5
522 Ma (Phase II_c). The SST rises by ~ 7°C (23°C to 30°C) (Keller and Lindinger, 1989), showing
523 a rough comparison although uncertainties occur at some age variation boundaries between
524 the two proxies.

525 Overall, the post-K/PgB longer-term trend of terrestrial climate cycles is closely
526 comparable to coeval changes of SST estimated from $\delta^{18}O$ values of planktonic foraminifera
527 (Jung et al., 2013) and TEX_{86} (Vellekoop et al., 2016; Woelders et al., 2017), and to the
528 Maastrichtian BWT estimated from benthic foraminifera $\delta^{18}O$ data (e.g., Hollis et al., 2012;
529 Barnet et al., 2018, 2019). The similarity between the pCO_2 trend, SST and BWT indicates
530 that consistent longer-term global climate change occurred in both terrestrial and surface
531 ocean environments during the early Paleocene.

532 However, BWT appears to become decoupled the deep ocean temperature from surface
533 ocean and terrestrial realms during Phase II and III. That is the post-K/PgB vibration in pCO_2
534 and SST are accompanied by a coeval longer-term rise in BWT in the aftermath of the
535 end-Cretaceous extinction till 62.5 Ma (Fig. 6D), representing a major decoupling between
536 the surface and deep ocean during times of rapid but transient climate change, pCO_2 turnover
537 and volcanic pulse. As discussed before, the release of significant quantities of sulfate
538 aerosols during Deccan Traps outgassing may be sufficient to counteract the warming effects
539 of rising pCO_2, with a potential decrease of global surface temperature by ~4.5°C from a
540 single pulse of decade-long Deccan Traps eruptions (Schmidt et al., 2016), but such a cooling
541 effect would only be short-term and would not affect longer-term climatic evolution due to the
542 extremely short residence time (~50 years) of sulfate aerosols in the atmosphere (Kring, 2003;
543 Galeotti et al., 2004; Schmidt et al., 2016). The sulfate aerosols would be then considered as
544 instantaneous in terms of geological time and are almost impossible to be preserved or
545 recognized in the geological record. Such extremely short-lived events are unlikely to be
546 recorded even in high-resolution paleothermometry studies, where decadal-centennial
547 sampling is extremely difficult to make (Schmidt et al., 2016; Bond and Sun, 2021).
548 Accordingly, the bolide impact winter would have led to an instantaneous cooling. Therefore,
549 we suggest that Deccan Traps volcanism and Chicxulub impact perturbed global climate
550 immediately after the K/PgB), but did not have a significant effect on longer-term climate.
551 That is to say, the they would not be the key factors that caused the longer-term vibration in
552 pCO_2 and SST and secular rise in BWT in the aftermath of the end-Cretaceous extinction.

553 Integrating the evolution of terrestrial $\delta^{13}C$ and pCO_2 with marine $\delta^{13}C$, BWT and SST,
554 we propose that the climate and environment have a rapidly and vibrantly change during the
555 interval of ~1.5 Myr (66.0−64.5 Ma) after the end-Cretaceous mass-extinction. Proxies of

carbon isotope, pCO_2 and SST show a pattern of dramatic reduction, short smooth towards rapid rebound, unraveling a process of deterioration, stabilization and recovery for the longer-term global ecosystem and climate, likely representing the response to carbon cycle perturbation.

It is proposed that the ecosystem recovery was fast, erratic and unstable in the terrestrial and surface ocean ecosystems, but slow and stable in the deep sea. Alternatively, climate and environmental perturbation may have been much more significant in the surface ocean and terrestrial realm than in the deep sea, resulting in a relatively shorter and faster ecosystem recovery than expected in surface realms (e.g., ~1−2 Myr, Dessert et al., 2001; Donovan et al., 2016; or >3 Myr, D'Hondt et al., 1998; Adams and Mann, 2004). This may imply that the terrestrial and surface ocean realms were much more sensitive to climatic changes after the K/PgB than the deep ocean, which may have been relatively buffered due to the time lag for such major temperature changes to infiltrate into the deep sea; and the recovery capability of terrestrial ecosystems could be much more powerful than we expect (Keller et al., 2016). The changes in earth system processes likely correlating with patterns of pedogenic and marine fossil-test carbonate $\delta^{13}C$ values, pCO_2, and sea-water temperatures, suggest frameworks of feedback pathways are responsible for the comparable longer-term carbon cycle and temperature tendency in both terrestrial and marine ecosystems at the time.

Causal changes in the longer-term carbon cycle and climate invoke exchanges of carbon between Earth's crust, ocean, atmosphere and biosphere, involving complex processes of carbon burial, volcanism, weathering, organic matter oxidation, nutrient cycling, atmospheric CO_2 and O_2 (Berner, 2003), and others. When examining these processes prior to the K/PgB, fluctuations over timescales on the order of ~10 Myr in the relative rate of organic carbon burial and oxygen production (Berner, 2001, 2003; 2009), carbonate precipitation (Opdyke and Wilkinson, 1988; Li and Elderfield, 2013), island basalt and continental silicate weathering (Li and Elderfield, 2013), and oceanic ridge spreading (Muller et al., 2008) have been shown by modelling experiments. Following the K/PgB, long scale cycles were actually observed on the order of ~3−4 Myr in the relative rate of organic carbon burial (Berner, 2003), carbonate sedimentation (Opdyke and Wilkinson, 1988; Li and Elderfield, 2013), and continental sediment weathering (Li and Elderfield, 2013), which may not play key roles on the longer-term (~100−1000 Kyr) vibration of ecosystem and climate in the early aftermath of the end-Cretaceous extinction.

Conclusions

This study has expanded on the previous studies focused on pedogenic carbonate stable isotope and atmospheric CO_2 across the K/Pg boundary. New data and compiles show a similar vibration pattern of $\delta^{13}C$ in pedogenic and marine carbonates and of the reconstructed pCO_2 and SST with decoupling BWT.

Looking in more detail, three evolutionary phases (I−III) of carbon cycle and pCO_2 are distinguished: Phase I (70.0−66.0 Ma), II (66.0−63.5 Ma), III (63.5−62.3 Ma), and four stages (II_a−II_d) are further subdivided in Phase II, representing the key period of the climate and environment perturbation in the aftermath of the end-Cretaceous extinction. In the earliest

598 stage (II_a, 66.0−65.6 Ma), terrestrial $\delta^{13}C$ values greatly decline (HCC) and pCO_2 rapidly fall,
599 accompanied by significant changes in ecosystem and climate. The two proxies are relatively
600 constant for ~300 Kyr (II_b, 65.6−65.3 Ma) since then. Rebounding of $\delta^{13}C$ and pCO_2 quickly
601 finishes to the pre-K/PgB levels in a pan ~800 Kyr (II_c, 65.3−62.5 Ma). The pattern of $\delta^{13}C$
602 and pCO_2 change reveals a vibrant process of deterioration, stabilization and recovery for the
603 longer-term terrestrial ecosystem and environment, spanning ~1.5 Myr (66.0−64.5 Ma).

604 With comparison to the compiled marine records, $\delta^{13}C$ values of surface sea sediments
605 (fine fraction, nannoplankton, benthic foraminifera and marine bulk carbonate) and SST show
606 a quite similar pattern of the pedogenic $\delta^{13}C$ and pCO_2. However, $\delta^{13}C$ and BWT of benthic
607 foraminifera decouple the proxies in the surface ocean and terrestrial realms. That is, the
608 post-K/PgB variation in surface ocean and terrestrial $\delta^{13}C$, SST and pCO_2 is accompanied by
609 a coeval longer-term decease $\delta^{13}C$ and secular rise in BWT in deep ocean, representing a
610 major decoupling between the surface system and deep ocean during times of ecosystem and
611 climate changes. Together, these proxy changes suggest that the terrestrial and surface ocean
612 ecosystems and climates experienced an unstable, much more unpredictable and erratic
613 recovery process than the deep ocean in the aftermath of the end-Cretaceous extinction.

614 Besides triggering in the end-Cretaceous extinction, Deccan Traps volcanism and
615 Chicxulub impact perturbed global instantaneous environment and climate immediately after
616 the K/PgB, in extremely short time (<~1.0 Kyr), leading to transient collapse of primary
617 productivity, surface water acidification, release of methane hydrate, etc.; but did not have a
618 significant effect on longer-term (>~100 Kyr) climate. Namely, the two events would not be
619 the key factors that caused the longer-term vibration in $\delta^{13}C$, pCO_2 and SST as well as secular
620 rise in BWT in the aftermath of the end-Cretaceous extinction. In particular, the HCC and
621 pCO_2 fall after the K/PgB is at odds with the expected positive shift and rise in pCO_2
622 following the Deccan Traps and Chicxulub impact.

623

624 **Acknowledgements**

625 We thank the reviewers for their helpful comments and constructive suggestions. Dr.
626 James. Barnet is grateful for the revision of some key knowledge and language polishment in
627 the early version of the manuscript. Dr. Yuan Gao helps make the Kernel smoothing of data,
628 Mr Yong Zhou took part in the field work in early time. It is acknowledged this research was
629 supported by the National Natural Science Foundation of China (NSFC grants 42172106 and
630 41372016).

631 The supporting information files (Text S1 and Tables S1−S3) are deposited and can be
632 found in the repository of Figshare (https://figshare.com/s/a75143bb6874e231d82c) or DOI:
633 10.6084/m9.figshare.19649739 when this article is accepted for publication.

634

635 **References**

636 Adams, J. B., Mann, M. E., & D'Hondt, S. (2004). The Cretaceous-Tertiary extinction:
637 Modeling carbon flux and ecological response. *Paleoceanography, 19*, PA1002.

https://doi.org/10.1029/2002PA000849.
Alegret, L., & Thomas, E. (2013). Benthic foraminifera across the Cretaceous/Paleogene boundary in the Southern Ocean (ODP Site 690): Diversity, food and carbonate saturation. *Marine Micropaleontology, 105*, 40–51.
Alegret, L., Thomas, E., & Lohmann, K. C. (2012). End-Cretaceous marine mass extinction not caused by productivity collapse. *Proceedings of the National Academy of Sciences, 109*(3), 728−732. https://doi.org/10.1073/pnas.1110601109
Alvarez, L. W., Alvarez, W., Asaro, F., & Michel, H. V. (1980). Extraterrestrial Cause for the Cretaceous-Tertiary Extinction - Experimental Results and Theoretical Interpretation. *Science, 208*(4448), 1095−1108. https://doi.org/10.1126/science.208.4448.1095.
Arens, N. C., & Jahren, A. H. (2000). Carbon isotope excursion in atmospheric CO_2 at the Cretaceous-Tertiary boundary: Evidence from terrestrial sediments. *Palaios, 15*(4), 314−322. https://doi.org/10.2307/3515539
Arens, N. C., Jahren, A. H., & Amundson, R. (2000). Can C3 plants faithfully record the carbon isotopic composition of atmospheric carbon dioxide? *Paleobiology, 26*(1), 37-164.
Arreguín-Rodríguez, G. J., Barnet, J. S. K., Leng, M. J., Littler, K., Kroon, D., Schmidt, D. N., Thomas, E., & Alegret, L. (2021). Benthic foraminiferal turnover across the Dan-C2 event in the eastern South Atlantic Ocean (ODP Site 1262). *Palaeogeography, Palaeoclimatology, Palaeoecology, 572*, 110410. https://doi.org/10.1016/j.palaeo.2021.110410
Barnet, J. S. K., Littler, K., Kroon, D., Leng, M. J., Westerhold, T., Röhl, U., & Zachos, J. C. (2018). A new high-resolution chronology for the late Maastrichtian warming event: Establishing robust temporal links with the onset of Deccan volcanism. *Geology, 46*(2), 147-150. https://doi.org/10.1130/G39771.1
Barnet, J. S. K., Littler, K., Westerhold, T., Kroon, D., Leng, M. J., Bailey, I., Röhl, U., & Zachos, J. C. (2019). A High-Fidelity Benthic Stable Isotope Record of Late Cretaceous–Early Eocene Climate Change and Carbon-Cycling. *Paleoceanography and Paleoclimatology, 34*(4), 672−691. https://doi.org/10.1029/2019PA003556
Beerling, D. J., Lomax, B. H., Royer, D. L., Upchurch, G. R., & Kump, L. R. (2002). An atmospheric pCO_2 reconstruction across the Cretaceous-Tertiary boundary from leaf megadossils. *Proceedings of the National Academy of Sciences, 99*(12), 7836–7840.
Berner, R. A. (2001). Modelling atmospheric O_2 over Phanerozoic time. *Geochimica et Cosmochimica Acta, 65*, 685-694
Berner, R. A. (2003). The long-term carbon cycle, fossil fuels and atmospheric composition. *Nature, 426*(6964), 323−326. https://doi.org/10.1038/nature02131
Berner, R. A. (2009). Phanerozoic atmospheric oxygen: new results using the GEOCARBSULF model. *American Journal of Science, 309*, 603–606. https://doi.org/doi:10.2475/07.2009.03
Bond, D. P. G., & Sun, Y. D. (2021). Global Warming and Mass Extinctions Associated With Large Igneous Province Volcanism. In R. E. Ernst, A. J. Dickson, & A. Bekker (Eds.), *Large Igneous Provinces: A Driver of Global Environmental and Biotic Changes* (pp. 85–102): Geophysical Monograph Series.
Boucot, A. J., Chen, X., Scotese, C. R., & Morley, R. J. (Cartographer). (2013). Phanerozoic

682 Paleoclimate: An Atlas of Lithologic Indicators of Climate
683 Bown, P. (2005). Selective calcareous nannoplankton survivorship at the Cretaceous-Tertiary
684 boundary. *Geology, 33*, 653–656.
685 Breecker, D. O., & Retallack, G. (2014). Refining the pedogenic carbonate atmospheric CO_2
686 proxy and application to Miocene CO_2. *Palaeogeography, Palaeoclimatology,*
687 *Palaeoecology, 406*, 1−8. https://doi.org/10.1016/j.palaeo.2014.04.012
688 Breecker, D. O., & Sharp, Z. D. (2008). A field and laboratory method for monitoring the
689 concentration and isotopic composition of soil CO_2. *Rapid Communications in Mass*
690 *Spectrometry, 22*(4), 449−454. https://doi.org/10.1002/rcm.3382
691 Breecker, D. O., Sharp, Z. D., & McFadden, L. D. (2009). Seasonal bias in the formation and
692 stable isotope composition of pedogenic carbonate in modern soil from central New
693 Mexico, USA. *Geological Society of America Bulletin, 121*, 630−640.
694 Breecker, D. O., Sharp, Z. D., & McFadden, L. D. (2010). Atmospheric CO_2 concentrations
695 during ancient greenhouse climates were similar to those predicted for AD 2100.
696 *Proceedings of the National Academy of Sciences of the United States of America,*
697 *107*(2), 576−580. https://doi.org/10.1073/pnas.0902323106
698 Brook, G. A., Folkoff, M. E., & Box, E. O. (1983). A World Model of Soil Carbon-Dioxide.
699 *Earth Surface Processes and Landforms, 8*(1), 79−88.
700 https://doi.org/10.1002/esp.3290080108
701 Cerling, T. E. (1991). Carbon dioxide in the atmosphere; evidence from Cenozoic and
702 Mesozoic Paleosols. *American Journal of Science, 291*(4), 377−400.
703 https://doi.org/10.2475/ajs.291.4.377
704 Cerling, T. E. (1999). Stable Carbon Isotopes in Palaeosol Carbonates. In M. Thiry & R.
705 Simon-Coincon (Eds.), *Palaeoweathering, palaeosurfaces and related continental*
706 *deposits* (Vol. 27, pp. 43−60): Blackwell, Oxford, International.
707 Clyde, W. C., Ting, S. Y., Snell, K. E., Bowen, G. J., Tong, Y. S., Koch, P. L., Li, Q., &
708 Wang, Y. Q. (2010). New Paleomagnetic and Stable-Isotope Results from the
709 Nanxiong Basin, China: Implications for the K/T Boundary and the Timing of
710 Paleocene Mammalian Turnover. *Journal of Geology, 118*(2), 131−143.
711 https://doi.org/10.1086/649893
712 Coccioni, R., Bancalà, G., Catanzarit, R., Fornaciari, E., Frontalini, F., Giusberti, L., Jovane,
713 L., Luciani, V., et al. (2012). An integrated stratigraphic record of the Palaeocene–
714 lower Eocene at Gubbio (Italy): New insights into the early Palaeogene hyperthermals
715 and carbon isotope excursions. *Terra Nova, 24*, 380–386.
716 https://doi.org/10.1111/j.1365-3121.2012.01076.x
717 Coccioni, R., & Marsili, A. (2007). The response of benthic foraminifera to the K–Pg
718 boundary biotic crisis at Elles (northwestern Tunisia). *Palaeogeography,*
719 *Palaeoclimatology, Palaeoecology, 255*(1−2), 157−180.
720 https://doi.org/10.1016/j.palaeo.2007.02.046
721 Cohen, K. M., Finney, S. C., Gibbard, P. L., & Fan, J. X. (2013). The ICS International
722 Chronostratigraphic Chart *36*, 199–204.
723 Cohen, K. M., Harper, D. A. T., Gibbard, P. L., & Fan, J. X. (2022). International
724 Chronostratigraphic Chart. In: International Commission on Stratigraphy.
725 D'Hondt, S., & Keller, G. (1991). Some patterns of planktic foraminiferal assemblage

turnover at the Cretaceous-Tertiary boundary. *Marine Micropaleontology, 17*, 77–118.
D'Hondt, S., Pilson, M. E. Q., Sigurdsson, H., Hanson, A. K., & Carey, S. (1994). Surface-water acidification and extinction at the Cretaceous-Tertiary boundary. *Geology, 22*, 983–986.
Dessert, C., Dupre, B., Francois, L. M., Schott, J., Gaillardet, J., Chakrapani, G., & Bajpai, S. (2001). Erosion of Deccan Traps determined by river geochemistry: impact on the global climate and the Sr^{87}/Sr^{86} ratio of seawater. *Earth and Planetary Science Letters, 188*(3−4), 459−474. https://doi.org/10.1016/S0012-821x(01)00317-X
D'Hondt, S., Donaghay, P., Zachos, J. C., Luttenberg, D., & Lindinger, M. (1998). Organic carbon fluxes and ecological recovery from the Cretaceous-Tertiary mass extinction. *Science, 282*(5387), 276−279. https://doi.org/10.1126/science.282.5387.276
Donovan, M. P., Iglesias, A., Wilf, P., Labandeira, C. C., & Cúneo, N. R. (2016). Rapid recovery of Patagonian plant–insect associations after the end-Cretaceous extinction. *Nature Ecology & Evolution, 1*(1), 0012. https://doi.org/10.1038/s41559-016-0012
Dworkin, S. I., Nordt, L., & Atchley, S. (2005). Determining terrestrial paleotemperatures using the oxygen isotopic composition of pedogenic carbonate. *Earth and Planetary Science Letters, 237*(1–2), 56–68. https://doi.org/10.1016/j.epsl.2005.06.054
Dzombak, R. M., Sheldon, N. D., Mohabey, D. M., & Samant, B. (2020). Stable climate in India during Deccan volcanism suggests limited influence on K–Pg extinction. *Gondwana Research, 85*, 19–31. https://doi.org/10.1016/j.gr.2020.04.007
Ekart, D. D., Cerling, T. E., Montanez, I. P., & Tabor, N. J. (1999). A 400 million year carbon isotope record of pedogenic carbonate: Implications for paleoatmospheric carbon dioxide. *American Journal of Science, 299*(10), 805−827. https://doi.org/10.2475/ajs.299.10.805
Eldrett, J. S., Vieira, M., Gallagher, L., Hampton, M., Blaauw, M., & Swart, P. K. (2021). Late Cretaceous to Palaeogene carbon isotope, calcareous nannofossil and foraminifera stratigraphy of the Chalk Group, Central North Sea. *Marine and Petroleum Geology, 124*, 104789. https://doi.org/10.1016/j.marpetgeo.2020.104789
Erben, H. K., Ashraf, A. R., Böhm, H., Hahn, G., Hambach, U., Krumsiek, K., Stets, J., Thein, J., et al. (1995). Die Kreide/Tertiär-Grenze im Nanxiong-Becken (Kontinentalfazies, Südostchina). *Erdwissenschaftliche Forschung, 32*, 1–245.
Galeotti, S., Brinkhuis, H., & Huber, M. (2004). Records of post–Cretaceous-Tertiary boundary millennial-scale cooling from the western Tethys: A smoking gun for the impact-winter hypothesis? *Geology, 32*(6). https://doi.org/doi:10.1130/G20439.1
Gao, Y., Ibarra, D. E., Caves Rugenstein, J. K., Chen, J. Q., Kukla, T., Methner, K., Gao, Y. f., Huang, H. Y., et al. (2021). Terrestrial climate in mid-latitude East Asia from the latest Cretaceous to the earliest Paleogene: A multiproxy record from the Songliao Basin in northeastern China. *Earth-Science Reviews, 216*, 103572. https://doi.org/10.1016/j.earscirev.2021.103572
Gao, Y., Ibarra, D. E., Wang, C. S., Caves, J. K., Chamberlain, C. P., Graham, S. A., & Wu, H. S. (2015). Mid-latitude terrestrial climate of East Asia linked to global climate in the Late Cretaceous. *Geology, 43*(4), 287–290. https://doi.org/10.1130/G36427.1
Gertsch, B., Keller, G., Adatte, T., Garg, R., Prasad, V., Berner, Z., & Fleitmann, D. (2011). Environmental effects of Deccan volcanism across the Cretaceous-Tertiary transition

in Meghalaya, India. *Earth and Planetary Science Letters, 310*, 272–285.
Gilabert, V., Arenillas, I., Arz, J. A., Batenburg, S. J., & Robinson, S. A. (2021a). . Multiproxy analysis of paleoenvironmental, paleoclimatic and paleoceanographic changes during the early Danian in the Caravaca section (Spain). *Palaeogeography, Palaeoclimatology, Palaeoecology, 576*, 110513. https://doi.org/doi.org/10.1016/j.palaeo.2021.110513
Gilabert, V., Batenburg, S. J., Arenillas, I., & Arz, J. A. (2021b). Contribution of orbital forcing and Deccan volcanism to global climatic and biotic changes across the Cretaceous-Paleogene boundary at Zumaia, Spain. *Geology, 50*, 21–25. https://doi.org/https://doi.org/10.1130/G49214.1
Gu, X., Zhang, L. M., Yin, R. S., Grasby, S. E., Yao, H. W., Tan, J., & Wang, C. S. (2022). Deccan volcanic activity and its links to the end-Cretaceous extinction in northern China *Global and Planetary Change, 210*, 103772.
Harper, D. T., Suarez, M. B., Uglesich, J., You, H. L., Li, D. Q., & Dodson, P. (2021). Aptian-Albian clumped isotopes from northwest China: cool temperatures, variable atmospheric pCO_2 and regional shifts in the hydrologic cycle. *Climate of the Past, 17*(4), 1607–1625. https://doi.org/10.5194/cp-17-1607-2021
Hart, M. B., Leighton, A. D., Hampton, M. C., & Smart, W. (2019). Global bioevents and the Cretaceous/Paleogene boundary in Texas and Alabama: Stratigraphy, correlation and ocean acidification. *Global and Planetary Change, 175*, 129–143.
Henehan, M. J., Hull, P. M., Penman, D. E., Rae, J. W., & Schmidt, D. N. (2016). Biogeochemical significance of pelagic ecosystem function: an end-Cretaceous case study. *Philos Trans R Soc Lond B Biol Sci, 371*(1694). https://doi.org/10.1098/rstb.2015.0510
Henehan, M. J., Ridgwell, A., Thomas, E., Zhang, S., Alegret, L., Schmidt, D. N., Rae, J. W. B., Witts, J. D., et al. (2019). Rapid ocean acidification and protracted Earth system recovery followed the end-Cretaceous Chicxulub impact. *Proceedings of the National Academy of Sciences, 116*(45), 22500–22504. https://doi.org/10.1073/pnas.1905989116
Hildebrand, A. R., Penfield, G. T., Kring, D. A., Pilkington, M., Camargo, A., Jacobsen, S. B., & Boynton, W. V. (1991). Chicxulub Crater - a Possible Cretaceous Tertiary Boundary Impact Crater on the Yucatan Peninsula, Mexico. *Geology, 19*(9), 867–871. https://doi.org/10.1130/0091-7613(1991)019<0867:Ccapct>2.3.Co;2
Hollis, C. J., Taylor, K. W. R., Handley, L., Pancost, R. D., Huber, M., Creech, J. B., Hines, B. R., Crouch, E. M., et al. (2012). Early Paleogene temperature history of the southwest Pacific Ocean: Reconciling proxies and models. *Earth and Planetary Science Letters, 349–350*, 53–66. https://doi.org/doi:10.1016/j.epsl.2012.06.024
Huang, C. M., Retallack, G. J., & Wang, C. S. (2012). Early Cretaceous atmospheric pCO_2 levels recorded from pedogenic carbonates in China. *Cretaceous Research, 33*, 42–49.
Huang, C. M., Retallack, G. J., Wang, C. S., & Huang, Q. H. (2013). Paleoatmospheric pCO_2 fluctuations across the Cretaceous-Tertiary boundary recorded from paleosol carbonates in NE China. *Palaeogeography, Palaeoclimatology, Palaeoecology, 385*, 95–105. https://doi.org/10.1016/j.palaeo.2013.01.005
Hull, P. M., Bornemann, A., Penman, D. E., Henehan, M. J., Norris, R. D., Wilson, P. A.,

Blum, P., Alegret, L., et al. (2020). On impact and volcanism across the Cretaceous-Paleogene boundary. *Science, 367*(6475), 266–272. https://doi.org/10.1126/science.aay5055

Hull, P. M., & Norris, R. D. (2011). Diverse patterns of ocean export productivity change across the Cretaceous-Paleogene boundary: New insights from biogenic barium. *Paleoceanography, 26*, PA3205.

Hsü, K. J., & Mackenzie, F. (1985). "A "Strangelove" ocean in the earliest Tertiary" in The Carbon Cycle and Atmospheric CO_2: Natural Variations Archean to Present. In E. T. Sundquist & W. S. Broecker (Eds.), *Geophysical Monograph Series* (pp. 487–492). Washington, D.C: American Geophysical Union. Imbellone, P. A. (2011). Classification of Paleosols. São Paulo, UNESP. *Geociências, 30*(1), 5–13.

Jung, C., Voigt, S., Friedrich, O., Koch, M. C., & Frank, M. (2013). Campanian-Maastrichtian ocean circulation in the tropical Pacific. *Paleoceanography, 28*(3), 562–573. https://doi.org/10.1002/palo.20051

Keller, G. (1988). Extinction, Survivorship and Evolution of Planktic Foraminifera across the Cretaceous Tertiary Boundary at El-Kef, Tunisia. *Marine Micropaleontology, 13*(3), 239–263. https://doi.org/10.1016/0377-8398(88)90005-9

Keller, G. (2014). Deccan volcanism, the Chicxulub impact, and the end-Cretaceous mass extinction: Coincidence? Cause and effect? In *Volcanism, Impacts, and Mass Extinctions: Causes and Effects* (pp. 57–89): Geological Society of America, Special Paper.

Keller, G., Adatte, T., Bhowmick, P. K., Upadhyay, H., Dave, A., Reddy, A. N., & Jaiprakash, B. C. (2012). Nature and timing of extinctions in Cretaceous-Tertiary planktic foraminifera preserved in Deccan intertrappean sediments of the Krishnae Godavari Basin, India. *Earth and Planetary Science Letters, 341−344*, 211−221.

Keller, G., & Lindinger, M. (1989). Stable Isotope, Toc and $CaCO_3$ Record across the Cretaceous Tertiary Boundary at El-Kef, Tunisia. *Palaeogeography, Palaeoclimatology, Palaeoecology, 73*(3–4), 243–265. https://doi.org/10.1016/0031-0182(89)90007-2

Keller, G., Mateo, P., Monkenbusch, J., Thibault, N., Punekar, J., Spangenberg, J. E., Abramovich, S., Ashckenazi-Polivoda, S., et al. (2020). Mercury linked to Deccan Traps volcanism, climate change and the end-Cretaceous mass extinction. *Global and Planetary Change, 194*, 103312. https://doi.org/10.1016/j.gloplacha.2020.103312

Keller, G., Punekar, J., & Mateo, P. (2016). Upheavals during the Late Maastrichtian: Volcanism, climate and faunal events preceding the end-Cretaceous mass extinction. *Palaeogeography, Palaeoclimatology, Palaeoecology, 441*, 137–151. https://doi.org/10.1016/j.palaeo.2015.06.034

Khadkikar, A. S., Chamyal, L. S., & Ramesh, R. (2000). The character and genesis of calcrete in Late Quaternary alluvial deposits, Gujarat, western India, and its bearing on the interpretation of ancient climates. *Palaeogeography, Palaeoclimatology, Palaeoecology, 162*(3–4), 239–261. https://doi.org/10.1016/S0031-0182(00)00130-9

Kring, D. A. (2003). Environmental consequences of impact cratering events as a function of ambient conditions on Earth. *Astrobiology, 3*(1), 133–152.

Kring, D. A. (2007). The Chicxulub impact event and its environmental consequences at the

Cretaceous-Tertiary boundary. *Palaeogeography, Palaeoclimatology, Palaeoecology, 255*, 4–21.

Lee, Y. I. (1999). Stable isotopic composition of calcic paleosols of the Early Cretaceous Hasandong Formation, southeastern Korea. *Palaeogeography, Palaeoclimatology, Palaeoecology, 150*(1–2), 123–133. https://doi.org/10.1016/S0031-0182(99)00010-3

Li, G., Hirano, H., Batten, D. J., Wan, X. Q., Willems, H., & Zhang, X. Q. (2010). Biostratigraphic significance of spinicaudatans from the Upper Cretaceous Nanxiong Group in Guangdong, South China. *Cretaceous Research, 31*(4), 387–395. https://doi.org/10.1016/j.cretres.2010.05.003

Li, G. J., & Elderfield, H. (2013). Evolution of carbon cycle over the past 100 million years. *Geochimica et Cosmochimica Acta, 103*, 11–25. https://doi.org/10.1016/j.gca.2012.10.014

Li, J., Wen, X. Y., & Huang, C. M. (2016). Lower Cretaceous paleosols and paleoclimate in Sichuan Basin, China. *Cretaceous Research, 62*, 154-171. https://doi.org/10.1016/j.cretres.2015.10.002

Li, X. H., Chen, S. D., Cao, K., Chen, Y. H., Xu, B. L., & Ji, Y. N. (2009). Paleosols of the mid-Cretaceous: A report from Zhejiang and Fujian, SE China. *Earth Science Frontiers, 16*(5).

Li, X. H., Jenkyns, H. C., Zhang, C. K., Wang, Y., Liu, L., & Cao, K. (2014). Carbon isotope signatures of pedogenic carbonates from SE China: rapid atmospheric pCO_2 changes during middle-late Early Cretaceous time. *Geological Magazine, 151*(5), 830–849. https://doi.org/10.1017/S0016756813000897

Littler, K., Rohl, U., Westerhold, T., & Zachos, J. C. (2014). A high-resolution benthic stable-isotope record for the South Atlantic: Implications for orbital-scale changes in Late Paleocene-Early Eocene climate and carbon cycling. *Earth and Planetary Science Letters, 401*, 18–30. https://doi.org/10.1016/j.epsl.2014.05.054

Lomax, B., Beerling, D., G., U. J., & Otto-Bliesner, B. L. (2001). Rapid (10-yr) recovery of terrestrial productivity in a simulation study of the terminal Cretaceous impact event. *Earth and Planetary Science Letters, 192*, 137–144.

Ma, M. M., Liu, X. M., & Wang, W. Y. (2018). Palaeoclimate evolution across the Cretaceous-Palaeogene boundary in the Nanxiong Basin (SE China) recorded by red strata and its correlation with marine records. *Climate of the Past, 14*(3), 287–302. https://doi.org/10.5194/cp-14-287-2018

Ma, M. M., Zhang, W. Y., Zhao, M., Qiu, Y., Cai, H., Chen, J., & Liu, X. M. (2022). Deccan traps volcanism implicated in the extinction of non-avian dinosaurs in southeastern China. *Geophysical Research Letters, 49*, e2022GL100342. https://doi.org/https://doi.org/10.1029/2022GL100342

Machette, M. N. (1985). Calcic soils of the southwestern United States. *Soils and Quaternary Geology of the Southwestern United States*, 1–22. https://doi.org/10.1130/spe203-p1

Mack, G. H., James, W. C., & Monger, H. C. (1993). Classification of paleosols. *Geological Society of America Bulletin, 105*, 129–136.

MacLeod, N. (1998). Impacts and marine invertebrae extinctions. In M. M. Grady, R. Hutchison, G. J. H. McCall, & D. A. Rothery (Eds.), *Meteorites: Flux with Time and Impact Effects* (Vol. 140, pp. 217–246). London, United Kingdom: Geological

Society of London.
Milligan, J. N., Royer, D. L., Franks, P. J., Upchurch, G. R., & McKee, M. L. (2019). No evidence for a large atmospheric CO_2 spike across the Cretaceous-Paleogene boundary. *Geophysical Research Letters, 46*, 3462–3472. https://doi.org/https://doi.org/10.1029/2018GL081215
Muller, R. D., Sdrolias, M., Gaina, C., Steinberger, B., & Heine, C. (2008). Long-term sea-level fluctuations driven by ocean basin dynamics. *Science, 319*, 1357–1362.
Nordt, L., Atchley, S., & Dworkin, S. (2003). Terrestrial Evidence for Two Greenhouse Events in the Latest Cretaceous. *GSA Today, 13*(12), 4. https://doi.org/10.1130/1052-5173(2003)013<4:Teftge>2.0.Co;2
Nordt, L., Atchley, S., & Dworkin, S. I. (2002). Paleosol barometer indicates extreme fluctuations in atmospheric CO_2 across the Cretaceous-Tertiary boundary. *Geology, 30*(8), 703–706. https://doi.org/10.1130/0091-7613(2002)030<0703:Pbiefi>2.0.Co;2
Nordt, L., Dworkin, S., & Atchley, S. (2011). Biogeochemical and ecosystem behavior interpreted from Late Cretaceous and Early Paleocene paleosols and climates in the western interior of North America. *Geological Society of America Bulletin, 123*, 1745–1762.
Norouzi, M., Vaziri-Moghaddam, H., & Kalanat, B. (2021). Cretaceous–Paleogene transition interval in the north flank of the Alborz Mountains (N Iran); Planktic foraminiferal biostratigraphy and stable isotopes evidence. *Journal of African Earth Sciences, 183*, 104329. https://doi.org/10.1016/j.jafrearsci.2021.104329
Odin, G. S., Hurford, A. J., & Montanari, A. (1992). Study of a presumably volcano-sedimentary layer near the Cretaceous-Paleogene boundary in the Central Apennines (Italy). In G. S. Odin (Ed.), *Phanerozoic Time Scale: International Union of Geological Sciences Subcommission on Geochronology Bulletin de Liaison* (pp. 26–28).
Ogg, J. G., Hinnov, L. A., & Huang, C. (2012). Cretaceous. In F. M. Gradstein, J. G. Ogg, M. Schmitz, & G. Ogg (Eds.), *The Geologic Time Scale* (pp. 793–853). Oxford: Elsevier.
Ohno, S. (2014). Production of sulphate-rich vapour during the Chicxulub impact and implications for ocean acidification. *Nature Geoscience, 7*, 279–282.
Opdyke, B. N., & Wilkinson, B. H. (1988). Surface Area Control of Shallow Cratonic to Deep Marine Carbonate Accumulation. *Paleoceanography, 3*(6), 685–703. https://doi.org/10.1029/PA003i006p00685
Passey, B. H., & Cerling, T. E. (2002). Tooth enamel mineralization in ungulates: Implications for recovering a primary isotopic time-serie. *Geochimica et Cosmochimica Acta, 66*(18), 3225–3234. https://doi.org/10.1016/S0016-7037(02)00933-X
Percival, L. M. E., Jenkyns, H. C., Mather, T. A., Dickson, A. J., Batenburg, S. J., Ruhl, M., Hesselbo, S. P., Barclay, R., et al. (2018). Does large igneous province volcanism always perturb the mercury cycle? Comparing the records of Oceanic Anoxic Event 2 and the end-Cretaceous to other Mesozoic events. *American Journal of Science, 318*(8), 799–860. https://doi.org/10.2475/08.2018.01
Quillévéré, F., Norris, R. D., Kroon, D., & Wilson, P. A. (2008). Transient ocean warming and shifts in carbon reservoirs during the early Danian. *Earth and Planetary Science*

946 *Letters, 265*(3–4), 600–615. https://doi.org/https://doi.org/10.1016/j.epsl.2007.10.040
947 Renne, P. R., Deino, A. L., Hilgen, F. J., Kuiper, K. F., Mark, D. F., Mitchell, W. S., Morgan,
948 L. E., Mundil, R., et al. (2013). Time scales of critical events around the
949 Cretaceous-Paleogene boundary. *Science, 339*(6120), 684–687.
950 Retallack, G. J. (2001). *Soils of the Past--An Introduction to Paleopedolog*. Blackwell
951 Science Ltd, Oxford: Unwin Hyman.
952 Retallack, G. J. (2005). Pedogenic carbonate proxies for amount and seasonality of
953 precipitation in paleosols. *Geology, 33*(4), 333–336. https://doi.org/10.1130/G21263.1
954 Retallack, G. J. (2009). Refining a pedogenic-carbonate CO_2 paleobarometer to quantify a
955 middle Miocene greenhouse spike. *Palaeogeography, Palaeoclimatology,*
956 *Palaeoecology, 281*(1–2), 57–65. https://doi.org/10.1016/j.palaeo.2009.07.011
957 Robinson, S. A., Andrews, J. E., Hesselbo, S. P., Radley, J. D., Denni, P. F., Harding, I. C., &
958 Allen, P. (2002). Atmospheric pCO_2 and depositional environment from stable-isotope
959 geochemistry of calcrete nodules (Barremian, Lower Cretaceous, Wealden Beds,
960 England). *Journal of the Geological Society, 159*, 215–224.
961 https://doi.org/10.1144/0016-764901-015
962 Romanek, C. S., Grossman, E. L., & Morse, J. W. (1992). Carbon Isotopic Fractionation in
963 Synthetic Aragonite and Calcite - Effects of Temperature and Precipitation Rate.
964 *Geochimica et Cosmochimica Acta, 56*(1), 419–430.
965 https://doi.org/10.1016/0016-7037(92)90142-6
966 Sandler, A. (2006). Estimates of atmospheric CO_2 levels during the mid-Turonian derived
967 from stable isotope composition of paleosol calcite from Israel. In A. M. Alonso-Zarza
968 & L. H. Tanner (Eds.), *Paleoenvironmental Record and Applications of Calcretes and*
969 *Palustrine Carbonates* (pp. 75–88): Geological Society of America, Special Paper.
970 Schmidt, A., Skeffington, R. A., Thordarson, T., Self, S., Forster, P. M., Rap, A., Ridgwell,
971 A., Fowler, D., et al. (2016). Selective environmental stress from sulphur emitted by
972 continental flood basalt eruptions. *Nature Geoscience, 9*, 77–82.
973 Schoene, B., Eddy, M. P., Keller, C. B., & Samperton, K. M. (2021). An evaluation of
974 Deccan Traps eruption rates using geochronologic data. *Geochronology, 3*, 181–198.
975 https://doi.org/https://doi.org/10.5194/gchron-3-181-2021
976 Schoene, B., Eddy, M. P., Samperton, K. M., Keller, C. B., Keller, G., Adatte, T., & Khadri, S.
977 F. R. (2019). U-Pb constraints on pulsed eruption of the Deccan Traps across the
978 end-Cretaceous mass extinction. *Science, 363*(6429), 862-866.
979 https://doi.org/10.1126/science.aau2422
980 Schoene, B., Samperton, K. M., Eddy, M. P., Keller, G., Adatte, T., Bowring, S. A., Khadri, S.
981 F. R., & Gertsch, B. (2015). U-Pb geochronology of the Deccan Traps and relation to
982 the end-Cretaceous mass extinction. *Science, 347*(6218), 182–184.
983 https://doi.org/10.1126/science.aaa0118
984 Schulte, P., Alegret, L., Arenillas, I., Arz, J. A., Barton, P. J., Bown, P. R., Bralower, T. J.,
985 Christeson, G. L., et al. (2010). The Chicxulub Asteroid Impact and Mass Extinction
986 at the Cretaceous-Paleogene Boundary. *Science, 327*(5970), 1214–1218.
987 https://doi.org/10.1126/science.1177265
988 Scotese, C. R. (Cartographer). (2014). Atlas of Late Cretaceous Maps
989 Sepúlveda, J., Wendler, J. E., Summons, R. E., & Hinrichs, K.-U. (2009). Rapid resurgence of

marine productivity after the Cretaceous-Paleogene mass extinction. *Science, 326*, 129–132.

Shu, L. S., Zhou, X. M., Deng, P., Yu, X. Q., Wang, B., & Zu, F. P. (2014). Geological features and tectonic evolution of Meso-Cenozoic basins in southeastern China. *Geological Bulletin of China, 23*(9–10), 876–884 (in Chinese with English abstract).

Sinnesael, M., De Vleeschouwer, D., Coccioni, R., Claeys, P., Frontalini, F., Jovane, L., Savian, J. F., & Montanari, A. (2016). High-resolution multiproxy cyclostratigraphic analysis of environmental and climatic events across the Cretaceous-Paleogene boundary in the classic pelagic succession of Gubbio (Italy). In M. Menichetti, R. Coccioni, & A. Montanari (Eds.), *The Stratigraphic Record of Gubbio: Integrated Stratigraphy of the Late Cretaceous–Paleogene Umbria-Marche Pelagic Basin* (pp. 115–137): Geological Society of America Special Paper.

Spicer, R. A., & Collinson, M. E. (2014). Plants and floral change at the Cretaceous-Paleogene boundary: three decades on. In G. Keller & A. C. Kerr (Eds.), *Volcanism, Impacts, and Mass Extinctions: Causes and Effects. 505* (pp. 117–131): Geological Society of America Special Paper.

Sprain, C. J., Renne, P. R., Vanderkluysen, L., Pande, K., Self, S., & Mittal, T. (2019). The eruptive tempo of Deccan volcanism in relation to the Cretaceous-Paleogene boundary. *Science, 363*(6429), 866–870. https://doi.org/10.1126/science.aav1446

Soil Survey Staff. (1998). *Keys to Soil Taxonomy*. Blacksburg: Pocahontas Press.

Thibault, N., Husson, D., Harlou, R., Gardin, S., Galbrun, B., Huret, E., & Minoletti, F. (2012). Astronomical calibration of upper Campanian-Maastrichtian carbon isotope events and calcareous plankton biostratigraphy in the Indian Ocean (ODP Hole 762C): Implication for the age of the Campanian-Maastrichtian boundary. *Palaeogeography, Palaeoclimatology, Palaeoecology, 337*, 52–71. https://doi.org/10.1016/j.palaeo.2012.03.027

Tong, Y., Li, Q., & Wang, Y. Q. (2013). An Introduction to recent advance in the study of the continental Early Paleogene stages in China. *Journal of Stratigraphy, 37*, 428–440 (in Chinese with English abstract)

Tyrrell, T., Merico, A., & Armstrong McKay, D. I. (2015). Severity of ocean acidification following the end-Cretaceous asteroid impact. *Proceedings of the National Academy of Sciences, 112*, 6556–6561.

Vajda, V., McLoughlin, S. (2007). Extinction and recovery patterns of vegetation across the Cretaceous-Paleogene boundary – a tool for unraveling the causes of the end-Permian mass extinction. *Review of Palaeobotany and Palynology, 144*, 99–112.

Vajda, V., Raine, J. I., & Hollis, C. J. (2001). Indication of global deforestation at the Creataceous-Tertiary boundary by New Zealand fern spike. *Science, 294*(5547), 1700–1702. https://doi.org/10.1126/science.1064706

Vajda, V., Raine, J. I., Hollis, C. J., & Strong, C. P. (2003). Global effects of the Chicxulub asteroid impact on terrestrial vegetation-the palynological record from New Zealand K–T boundary. In P. Clayes (Ed.), *Impact Studies* (pp. 57−74). Berlin: Springer-Verlag.

Vandenberghe, N., Hilgen, F. J., Speijer, R. P., Ogg, J. G., Gradstein, F. M., Hammer, O., Hollis, C. J., & Hooker, J. J. (2012). The Paleogene Period. In F. M. Gradstein, O. J.G.,

S. M., & O. G. (Eds.), *The Geologic Time Scale* (pp. 855–921). Oxford: Elsevier B.V.

Vellekoop, J., Esmeray-Senlet, S., Miller, K. G., Browning, J. V., Sluijs, A., van de Schootbrugge, B., Damste, J. S. S., & Brinkhuis, H. (2016). Evidence for Cretaceous-Paleogene boundary bolide "impact winter" conditions from New Jersey, USA. *Geology, 44*(8), 619–622. https://doi.org/10.1130/G37961.1

Whittle, R. J., Witts, J. D., Bowman, V. C., Crame, J. A., Francis, A. E., & Ineson, J. (2019). Nature and timing of biotic recovery in Antarctic benthic marine ecosystems following the Cretaceous–Palaeogene mass extinction. *Palaeontology, 62*(6), 919–934.

Wilf, P., Johnson, K. R., & Huber, B. T. (2003). Correlated terrestrial and marine evidence for global climate chanaes before mass extinction at the Cretaceous-Paleogene boundary. *Proceedings of the National Academy of Sciences of the United States of America, 100*(2), 599–604. https://doi.org/10.1073/pnas.0234701100

Woelders, L., Vellekoop, J., Kroon, D., Smit, J., Casadio, S., Pramparo, M. B., Dinares-Turell, J., Peterse, F., et al. (2017). Latest Cretaceous climatic and environmental change in the South Atlantic region. *Paleoceanography, 32*(5), 466–483. https://doi.org/10.1002/2016pa003007

Wright, V. P. (1992). Paleosol Recognition: A guide to early diagenesis in terrestrial settings. *Development of Sedimentory, 47*, 591–619.

Zeebe, R. E., Westerhold, T., Littler, K., & Zachos, J. C. (2017). Orbital forcing of the Paleocene and Eocene carbon cycle. *Paleoceanography, 32*, 440–465. https://doi.org/10.1002/2016PA003054

Zhang, L. M., Wang, C. S., Wignall, P. B., Kluge, T., Wan, X. Q., Wang, Q., & Gao, Y. (2018). Deccan volcanism caused coupled pCO_2 and terrestrial temperature rises, and pre-impact extinctions in northern China. *Geology, 46*(3), 271–274. https://doi.org/10.1130/G39992.1

Zhang, X. Q., & Li, G. (2010). Discussion on geological age of the Pingling Member of Shanghu Formation in the Nanxiong Basin, Guangdong province. *Journal of Stratigraphy, 39*(1), 74–80 (in Chinese with English abstract).

Zhang, X. Q., Lin, J. N., Li, G., & Lin, Q. X. (2006). Non-marine Cretaceous-Paleogene boundary section at Datang, Nanxiong, northern Guangdong. *Journal of Stratigraphy, 30*, 327–340 (in Chinese with English abstract).

Zhang, X. Q., Zhang, X. M., Hou, M. C., Li, G., & Li, H. M. (2013). Lithostratigraphic subdivision of red beds in Nanxiong Basin, Guangdong, China. *Journal of Stratigraphy, 37*, 441–451 (in Chinese with English abstract).

Zhao, M. T., Ma, M. M., He, M., Qiu, Y. D., & Liu, X. M. (2021). Evaluation of the four potential Cretaceous-Paleogene (K-Pg) boundaries in the Nanxiong Basin based on evidences from volcanic activity and paleoclimatic evolution. *Science China-Earth Sciences, 64*(4), 631–641. https://doi.org/10.1007/s11430-020-9736-0

Zhao, Z. K., Mao, X. Y., Chai, Z. F., Yang, G. C., Zhang, F. C., & Yan, Z. (2009). Geochemical environmental changes and dinosaur extinction during the Cretaceous-Paleogene (K/T) transition in the Nanxiong Basin, South China: Evidence from dinosaur eggshells. *Chinese Science Bulletin, 54*(5), 806–815. https://doi.org/10.1007/s11434-008-0565-1

Zhao, Z. K., Ye, J., & Li, H. M. (1991). Extinction of the dinosaurs across the Cretaceous-Tertiary boundary in Nanxiong Basin, Guangdong Province. *Certebrata Palasiatica, 29*, 1–20.

References From the Supporting Information

Bemis, B. E., Spero, H. J., Bijma, J., & Lea, D. W. (1998). Reevaluation of the oxygen isotopic composition of planktonic foraminifera: Experimental results and revised paleotemperature equations. *Paleoceanography, 13*(2), 150−160. doi:10.1029/98pa00070

Berggren, W. A., Aubry, M. P., van Fossen, M., Kent, K. V., Norris, R. D., & Quillevere, F. (2000). Integrated Paleocene calcareous plankton magnetobiochronology and stable isotope stratigraphy: DSDP Site 384 (NW Atlantic Ocean). *Palaeogeography Palaeoclimatology Palaeoecology, 159*(1–2), 1–51. doi:10.1016/S0031-0182(00)00031-6

Boersma, A., Shackleton, N. J., Hall, M., & Given, Q. (1979). Carbon and oxygen isotope records at DSDP Site 384 (North Atlantic) and some Paleocene paleotemperatures and carbon isotope variations in the Atlantic Ocean. In A. Kaneps (Ed.), (pp. 695–717). TX, United States, Texas A & M University, Ocean Drilling Program, College Station: Initial Reports of the Deep Sea Drilling Project.

Cramer, B. S., Miller, K. G., Barrett, P. J., & Wright, J. D. (2011). Late Cretaceous-Neogene trends in deep ocean temperature and continental ice volume: Reconciling records of benthic foraminiferal geochemistry (delta O^{18} and Mg/Ca) with sea level history. *Journal of Geophysical Research-Oceans, 116*. doi:10.1029/2011jc007255

Dennis, K. J., Cochran, J. K., Landman, N. H., & Schrag, D. P. (2013). The climate of the Late Cretaceous: New insights from the application of the carbonate clumped isotope thermometer to Western Interior Seaway macrofossil. *Earth and Planetary Science Letters, 362*, 51−65. doi:10.1016/j.epsl.2012.11.036

Katz, M. E., Katz, D. R., Wright, J. D., Miller, K. G., Pak, D. K., Shackleton, N. J., & Thomas, E. (2003). Early Cenozoic benthic foraminiferal isotopes: Species reliability and interspecies correction factors. *Paleoceanography, 18*(2), 1024. doi:10.1029/2002pa000798

Larson, R. L., Steiner, M. B., Erba, E., & Lancelot, Y. (1990). Paleolatitudes and tectonic reconstructions of the oldest portion of the Pacific Plate; a comparative study. In L. H. Dearmont & N. K. McQuistion (Eds.), (pp. 615–631). TX, United States, Texas A & M University, Ocean Drilling Program, College Station: Initial Reports of the Deep Sea Drilling Project.

Lhomme, N., Clarke, G. K. C., & Ritz, C. (2005). Global budget of water isotopes inferred from polar ice sheets. *Geophysical Research Letters, 32*(20), L20502. doi:10.1029/2005gl023774

Shackleton, N. J., & Kennett, J. P. (1975). Paleotemperature history of the Cenozoic and the initiation of Antarctic glaciation; oxygen and carbon isotope analyses in DSDP sites 277, 279, and 281. *Initial Reports of the Deep Sea Drilling Project, 29*, 743–775.

Westerhold, T., Rohl, U., Donner, B., McCarren, H. K., & Zachos, J. C. (2011). A complete high-resolution Paleocene benthic stable isotope record for the central Pacific (ODP Site 1209). *Paleoceanography, 26*, PA2216. doi:10.1029/2010pa002092

Wilson, P. A., Norris, R. D., & Cooper, M. J. (2002). Testing the Cretaceous greenhouse hypothesis

using glassy foraminiferal calcite from the core of the Turonian tropics on Demerara Rise. *Geology, 30*(7), 607–610. doi:10.1130/0091-7613(2002)030<0607:Ttcghu>2.0.Co;2

Zachos, J. C., Stott, L. D., & Lohmann, K. C. (1994). Evolution of Early Cenozoic Marine Temperatures. *Paleoceanography, 9*(2), 353–387. doi:10.1029/93pa03266

Figure caption

Figure 1 Global climate zones laid over the K/PgB (~66 Ma) paleogeographic map (Scotese, 2014). Climate zones are modified from Boucot et al. (2013). Climate-sensitive sedimentary data are selected from those of the late Maastrichtian to project in the map, which is different from that of the Coniacian-Maastrichtian climatic zones in Boucot et al. (2013). The data marked as the Late Cretaceous are not chosen for the Maastrichtian zones. Please note, some climatic boundary lines are adjusted from the map in Boucot (2013). 1, Datang section, Nanxiong Basin, South China (this work); 2, core of Well Songke #1, Songliao Basin, Northeast China (Gao et al., 2015, 2021; Zhang et al., 2018); 3, Dawson Creek section of the Tornillo Basin. Big Bend National Park, Texas, USA (Nordt et al., 2003).

Figure 2 Geological sketches of the Nanxiong Basin with the location of the observed section. A, Geographical map of China showing the localities of study and citation sections. B, Geological sketch of the Nanxiong Basin. Geological map simplified from Shu et al. (2004). C, Geological sketch and transportation nearby the Datang section, Nanxiong, intercepted and simplified from Zhang et al. (2013).

Figure 3 Log of the Datang section, Nanxiong of Guangdong showing the stratigraphy, positions of calcrete samples and results of carbon and oxygen isotopes and estimated pCO_2. Magneto-chronostratigraphy are cited from Clyde et al. (2010) and lithostratigraphy and thickness from Zhang et al. (2006). Ages marked as red bold numbers aside the log are obtained by the chronostratigraphy chart (Ogg et al., 2012; Vandenberghe et al., 2012). Please note, the strongest negative excursion occurs at the K/PgB in the Datang section. Uncertainties (errors) of pCO_2 are produced from the subtraction from $S_{(z)}$=2000 ppmV at 25℃ using the method developed by Breecker and Retallack (2014) (details see section 4 in text).

Figure 4 Field paleosol photos and microscopic CL images from the upper Upper Cretaceous-Paleogene at the Datang section, Nanxiong, Guangdong province. A, Close-up view of calcisol with ginger-like and irregular calcretes at horizon of the sample DT-02, upper Zhutian Formation. B, Close-up view of calcisol with the calcrete at horizon of the sample DT-84, middle Shanghu Formation. C, CL image of the calcrete sample DT-55, lower Shanghu Formation. D, CL image of the calcrete sample DT-72, middle Shanghu Formation.

Figure 5 Crossplot of carbon and oxygen isotopes of the latest Cretaceous-earliest Paleogene pedogenic carbonates from the Datang section, Nanxiong Basin, South China.

Figure 6 Stable isotopes of terrestrial and marine carbonate, sea-water temperature and pCO_2 in the late Late Cretaceous-early Paleocene (~70−62 Ma). **A**, Carbon isotope of marine

fossil carbonates. **B**, Carbon isotope of pedogenic carbonates (details refer to Table S1−S2). **C**, pCO_2 estimated by carbon isotope of pedogenic carbonates (Table S1−S2). **D**, BWT and SST from ocean records (Text S1 and Table S3). Kernel smoothed time series (thick dark red dash lines) were calculated using a fixed 0.25 Myr bandwidth and using an Epanechnikov kernel centered on each data point. Note, three phases of carbon cycles and pCO_2 from terrestrial pedogenic carbonates are identified.

Figure 7 Comparison of $\delta^{13}C$, pCO_2 and SST across the K/PgB. Carbon isotopes of bulk carbonates marked as blue squares (ODP Site 1267, Walvis Ridge, South Atlantic) and grey circles (ODP Site U1403, J-Anomaly Ridge, North Atlantic) in the figure 7A are from Hull et al. (2020). Thick grey lines are five-point smoothed curves. The Deccan Trap ranges 66.3−65.6 Ma (Schoene et al., 2015, 2019) with a precise alternative $^{40}Ar/^{39}Ar$ age 66.413−65.422 Ma (dash line limitation with red arrow. Sprain et al., 2019) and corrected eruption rate (brownish red shadow area. Schoene et al., 2021). Other symbols and relevant data refer to Fig. 6.

Supplementary data caption

Text S1. Cited marine C-O isotopes and recalibrated seawater temperatures

Table S1. Details of samples, C-O isotope composition and pCO_2 of the latest Cretaceous-earliest Paleocene (~70−62 Ma) at Datang section, Nanxiong of Guangdong, SW China. GCD is the main part between Yangmeikeng and Huashuxia in the Datang section (Zhao et al., 1991).

Table S2. Details of samples, C-O isotope composition and pCO_2 of the latest Cretaceous-earliest Paleocene (~70−62 Ma) complied from GCD section, Nanxiong, S China; Songke Well #1, Songliao Basin, NE China and Dawson Creek, Texas, America

Table S3. C-O isotopes, SST and BWT of the latest Cretaceous-earliest Paleocene (~70−62 Ma)

Figure 1.

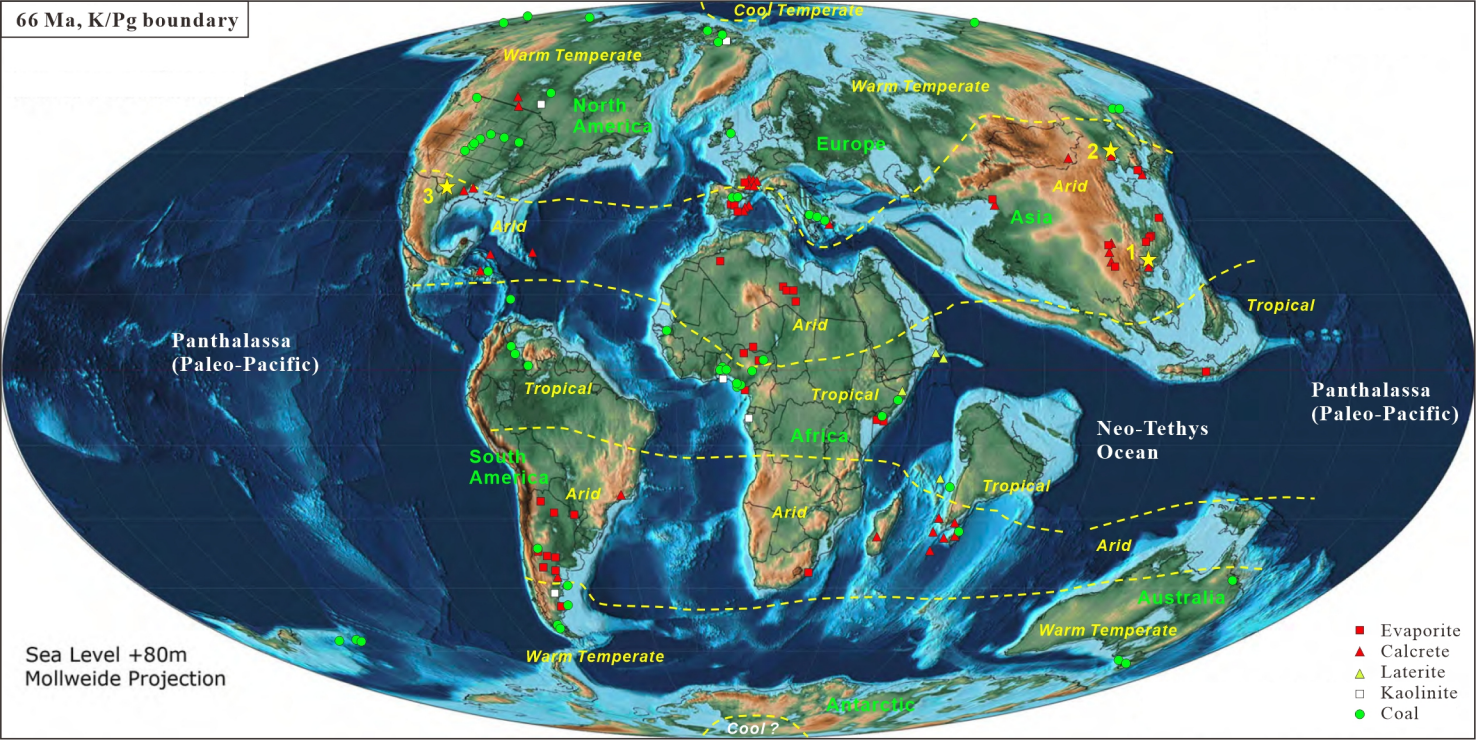
66 Ma, K/Pg boundary
Cool Temperate
Warm Temperate
North America
Warm Temperate
Europe
Arid
Asia
Arid
Tropical
Panthalassa (Paleo-Pacific)
Arid
Tropical
Tropical
Africa
Neo-Tethys Ocean
Panthalassa (Paleo-Pacific)
South America
Arid
Arid
Tropical
Arid
Australia
Warm Temperate
Warm Temperate
Antarctic
Cool ?
Sea Level +80m
Mollweide Projection
Evaporite
Calcrete
Laterite
Kaolinite
Coal

Figure 2.

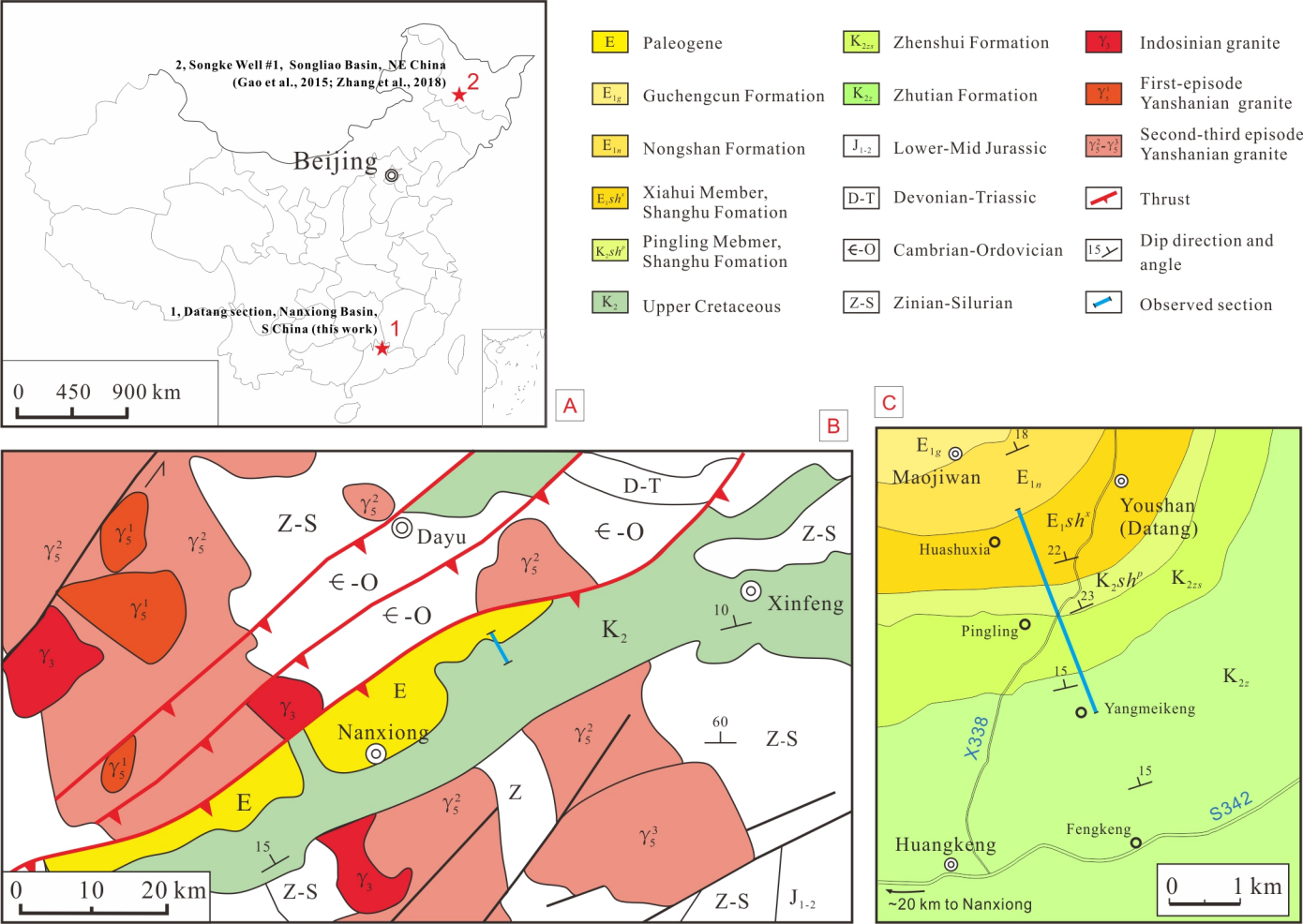
2, Songke Well #1, Songliao Basin, NE China
(Gao et al., 2015; Zhang et al., 2018)
2
Beijing
1, Datang section, Nanxiong Basin,
S China (this work)
1
0 450 900 km
A
E Paleogene
E1g Guchengcun Formation
E1n Nongshan Formation
E1sh Xiahui Member, Shanghu Fomation
K2sh Pingling Mebmer, Shanghu Fomation
K2 Upper Cretaceous
K2zs Zhenshui Formation
K2z Zhutian Formation
J1-2 Lower-Mid Jurassic
D-T Devonian-Triassic
∈-O Cambrian-Ordovician
Z-S Zinian-Silurian
γ3 Indosinian granite
γ5 1 First-episode Yanshanian granite
γ5 2-γ5 3 Second-third episode Yanshanian granite
Thrust
15 Dip direction and angle
Observed section
B
Z-S
Dayu
∈-O
∈-O
D-T
∈-O
Z-S
Xinfeng
10
K2
E
Nanxiong
60
Z-S
E
Z
15
Z-S
Z-S
J1-2
0 10 20 km
C
E1g
Maojiwan
18
E1n
Youshan
(Datang)
E1sh
Huashuxia
22
K2shp
K2zs
23
Pingling
15
K2z
Yangmeikeng
X338
15
S342
Fengkeng
Huangkeng
~20 km to Nanxiong
0 1 km

Figure 3.

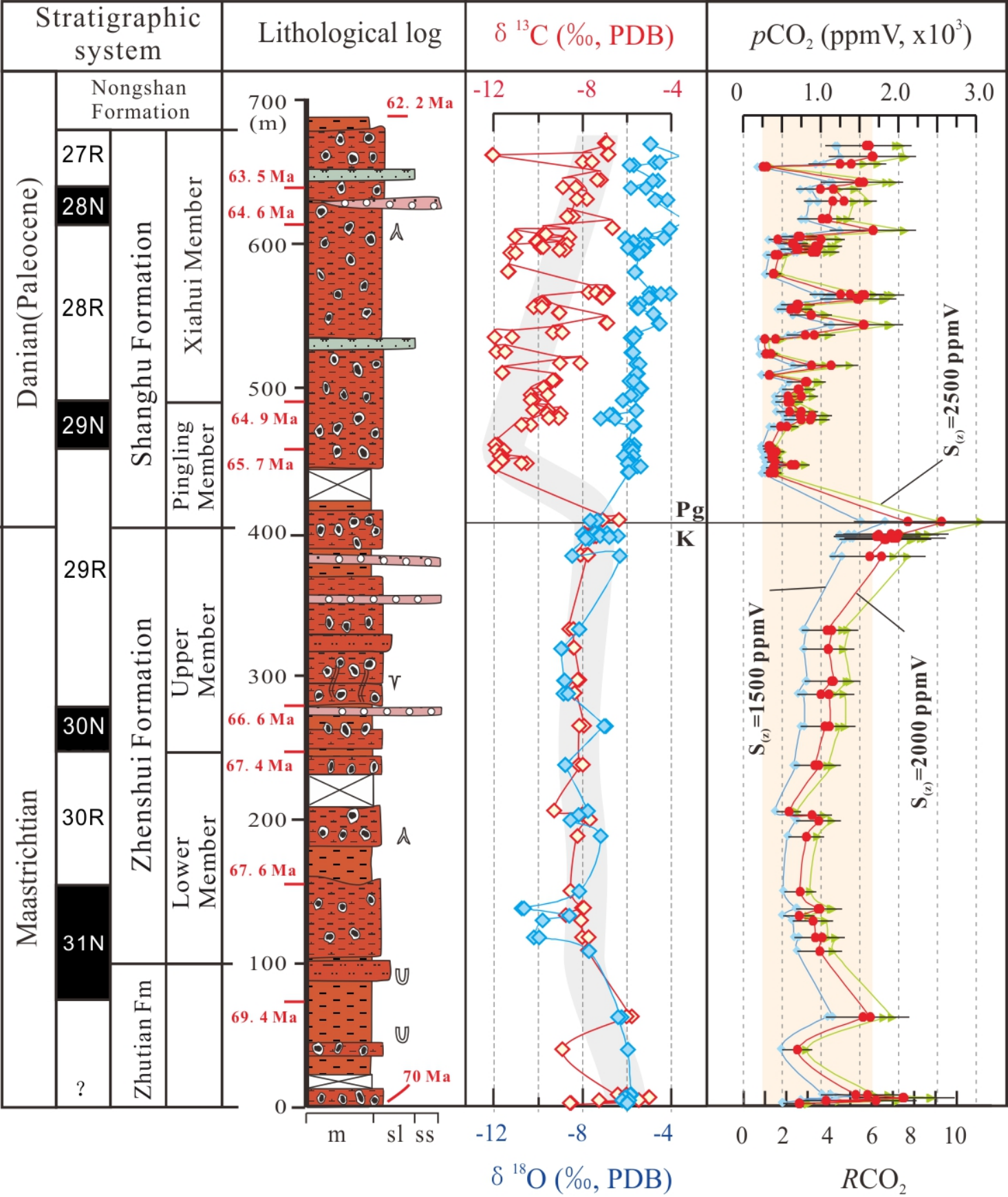
Stratigraphic system
Lithological log
δ 13C (‰, PDB)
pCO2 (ppmV, x10^3)
Danian(Paleocene)
Maastrichtian
Nongshan Formation
Shanghu Formation
Xiahui Member
Pingling Member
Zhenshui Formation
Upper Member
Lower Member
Zhutian Fm
27R
28N
28R
29N
29R
30N
30R
31N
?
700 (m)
600
500
400
300
200
100
0
62. 2 Ma
63. 5 Ma
64. 6 Ma
64. 9 Ma
65. 7 Ma
66. 6 Ma
67. 4 Ma
67. 6 Ma
69. 4 Ma
70 Ma
Pg
K
-12
-8
-4
0
1.0
2.0
3.0
S(z)=2500 ppmV
S(z)=1500 ppmV
S(z)=2000 ppmV
m
sl
ss
0
2
4
6
8
10
δ 18O (‰, PDB)
RCO2
Mudrock
Silty mudrock
Siltstone
Sandstone
Conglomerate
Paleosol with calcrete
Tube trace fossil
Rhizolith
Mudcrack
Leaching
29N
29R
Magnetic chron
Covered

Figure 4.

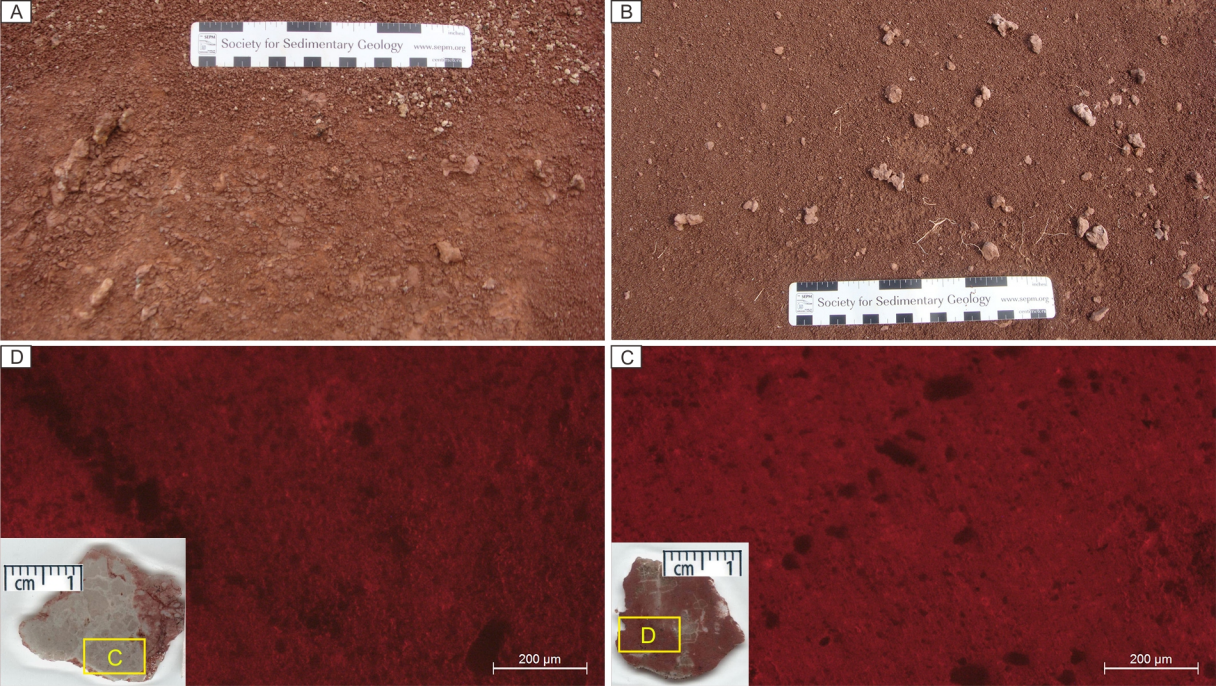
A
Society for Sedimentary Geology
www.sepm.org
B
Society for Sedimentary Geology
www.sepm.org
D
cm
1
C
200 µm
C
cm
1
D
200 µm

Figure 5.

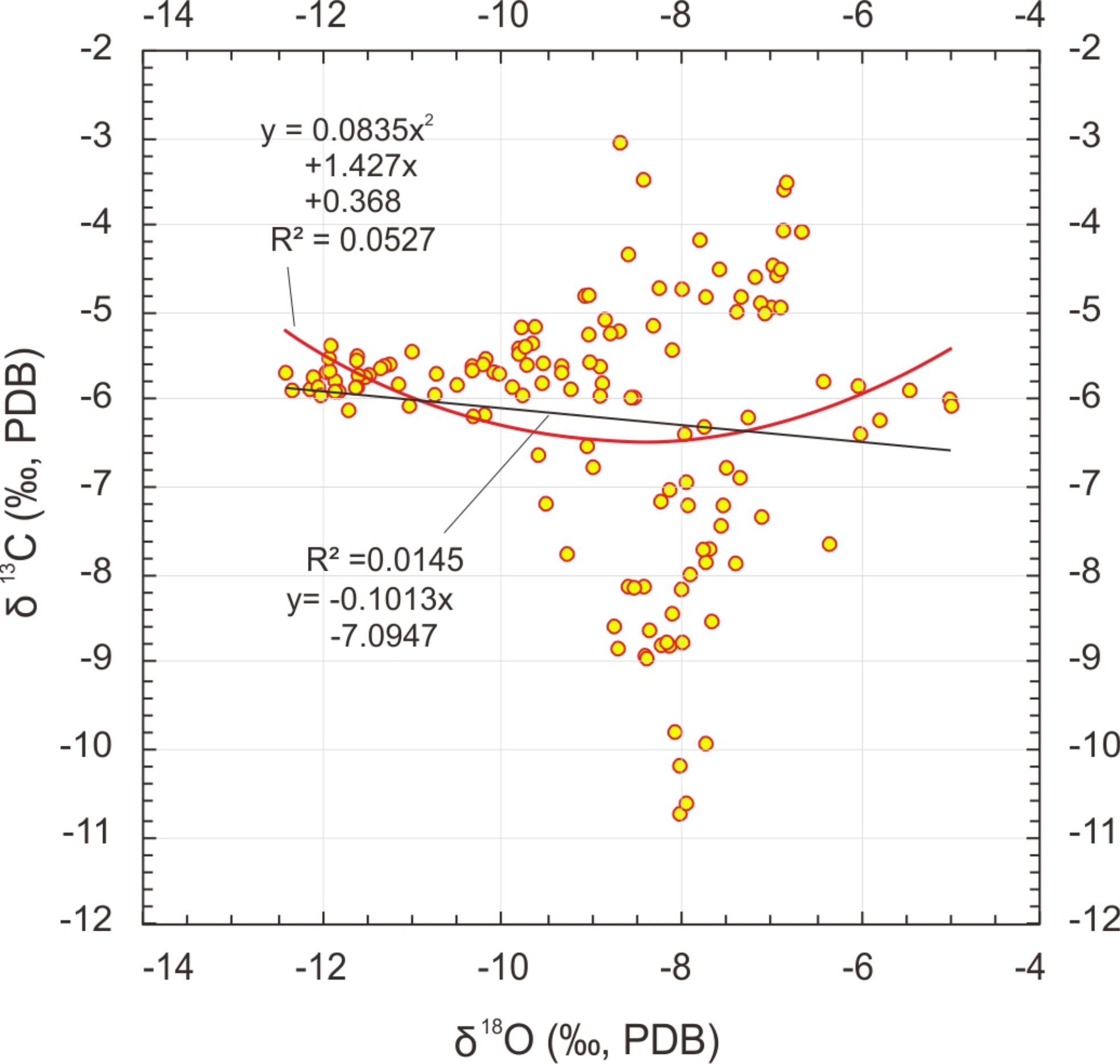
y = 0.0835x²
+1.427x
+0.368
R² = 0.0527
R² =0.0145
y= -0.1013x
-7.0947
δ 13C (‰, PDB)
δ 18O (‰, PDB)
-14
-12
-10
-8
-6
-4
-2
-3
-5
-7
-9
-11

Figure 6.

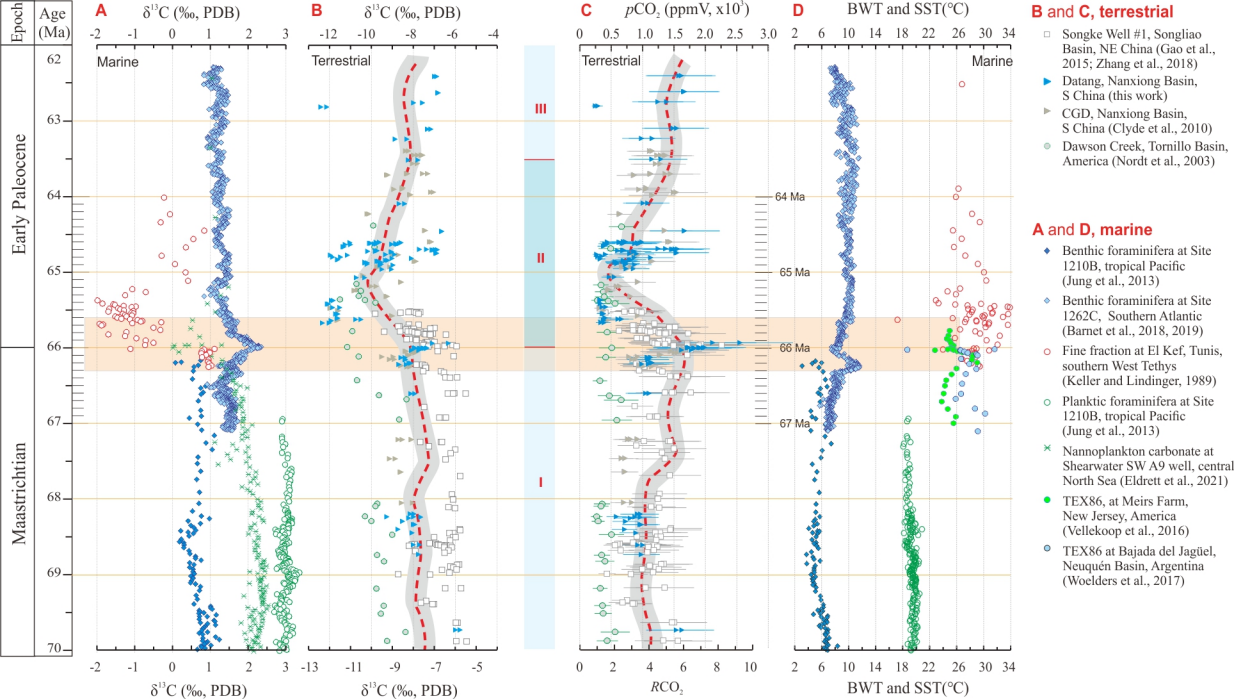
Epoch
Age (Ma)
Early Paleocene
Maastrichtian
A
δ13C (‰, PDB)
Marine
B
δ13C (‰, PDB)
Terrestrial
C
pCO2 (ppmV, x10³)
Terrestrial
D
BWT and SST(°C)
Marine
64 Ma
65 Ma
66 Ma
67 Ma
III
II
I
RCO2
B and C, terrestrial
Songke Well #1, Songliao Basin, NE China (Gao et al., 2015; Zhang et al., 2018)
Datang, Nanxiong Basin, S China (this work)
CGD, Nanxiong Basin, S China (Clyde et al., 2010)
Dawson Creek, Tornillo Basin, America (Nordt et al., 2003)
A and D, marine
Benthic foraminifera at Site 1210B, tropical Pacific (Jung et al., 2013)
Benthic foraminifera at Site 1262C, Southern Atlantic (Barnet et al., 2018, 2019)
Fine fraction at El Kef, Tunis, southern West Tethys (Keller and Lindinger, 1989)
Planktic foraminifera at Site 1210B, tropical Pacific (Jung et al., 2013)
Nannoplankton carbonate at Shearwater SW A9 well, central North Sea (Eldrett et al., 2021)
TEX86, at Meirs Farm, New Jersey, America (Vellekoop et al., 2016)
TEX86 at Bajada del Jagüel, Neuquén Basin, Argentina (Woelders et al., 2017)

Figure 7.

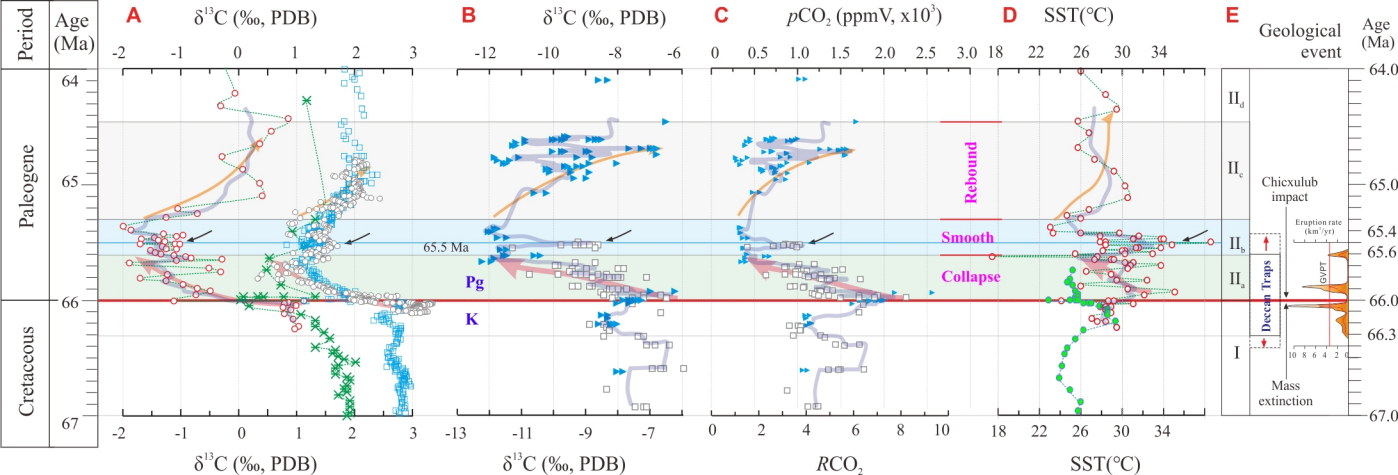
Period
Age (Ma)
Paleogene
Cretaceous
64
65
66
67
A
δ13C (‰, PDB)
-2 -1 0 1 2 3
B
δ13C (‰, PDB)
-12 -10 -8 -6
-13 -11 -9 -7
C
pCO2 (ppmV, x10^3)
0 0.5 1.0 1.5 2.0 2.5 3.0
0 2 4 6 8 10
RCO2
D
SST(°C)
18 22 26 30 34
SST(°C)
65.5 Ma
Pg
K
Rebound
Smooth
Collapse
E
Geological event
Age (Ma)
IId
IIc
IIb
IIa
I
Chicxulub impact
Deccan Traps
Eruption rate (km3/yr)
GVPT
10 8 6 4 2 0
Mass extinction
64.0
65.0
65.4
65.6
66.0
66.3
67.0